the dc rotation simply would have provided extra suppression by a uniform amount on top of the ac oscillation suppression, as illustrated by the purple dashed curve in Fig. 3B.

As the suppressed NCRIF and the enhanced dissipation under dc rotation are thought to be coming from vortex injection, this shared common origin could be vortices. If so, the competition between vortex injection and vortex motion is one possible explanation for this crossover. A large ac oscillation amplitude causes unpinning of the vortices; the oscillatory motion of these unpinned vortices overwhelms the effect of injected quantized vortices above a certain crossover ac oscillation speed. The gradual enhancement of the crossover speed is also seen with increasing dc speed and can be attributed to the larger number of unpinned vortices that are required to observe the crossover. We note that this oscillation amplitude is still very small, orders of magnitude smaller than the critical strain for the softening of solid helium.

The appearance of extra dissipation only at low temperatures is, however, puzzling, as vortex pinning is thought to be stronger at these temperatures (*24*). The lack of similarity to better-understood superfluids and the lack of a quantitative theory for supersolid vortices makes it difficult to explain this peculiar feature.

References and Notes

1. A. J. Leggett, *Phys. Rev. Lett.* **25**, 1543 (1970).
2. E. Kim, M. H. W. Chan, *Nature* **427**, 225 (2004).
3. E. Kim, M. H. W. Chan, *Science* **305**, 1941 (2004).
4. N. Prokof'ev, *Adv. Phys.* **56**, 381 (2007).
5. J. Day, T. Herman, J. Beamish, *Phys. Rev. Lett.* **95**, 035301 (2005).
6. J. Day, J. Beamish, *Phys. Rev. Lett.* **96**, 105304 (2006).
7. A. S. C. Rittner, W. Choi, E. J. Mueller, J. D. Reppy, *Phys. Rev. B* **80**, 224516 (2009).
8. M. W. Ray, R. B. Hallock, *Phys. Rev. Lett.* **100**, 235301 (2008).
9. M. W. Ray, R. B. Hallock, *Phys. Rev. B* **79**, 224302 (2009).
10. M. W. Ray, R. B. Hallock, *Phys. Rev. B* **82**, 012502 (2010).
11. M. W. Ray, R. B. Hallock, *Phys. Rev. Lett.* **105**, 145301 (2010).
12. Y. Aoki, H. Kojima, X. Lin, *Low Temp. Phys.* **34**, 329 (2008).
13. S. Kwon, N. Mulders, E. Kim, *J. Low Temp. Phys.* **158**, 590 (2009).
14. P. W. Anderson, *Nat. Phys.* **3**, 160 (2007).
15. Z. Nussinov, A. V. Balatsky, M. J. Graf, S. A. Trugman, *Phys. Rev. B* **76**, 014530 (2007).
16. C.-D. Yoo, A. T. Dorsey, *Phys. Rev. B* **79**, 100504 (2009).
17. J. Day, J. Beamish, *Nature* **450**, 853 (2007).
18. B. Hunt *et al.*, *Science* **324**, 632 (2009).
19. I. Iwasa, *Phys. Rev. B* **81**, 104527 (2010).
20. J. D. Reppy, *Phys. Rev. Lett.* **104**, 255301 (2010).
21. P. Gumann, N. Shimizu, A. Penzev, Y. Yasuta, M. Kubota, *J. Phys. Conf. Ser.* **150**, 032026 (2009).
22. T. Obata, M. Fukuda, N. Mikhin, J. D. Reppy, M. Kubota, *J. Low Temp. Phys.* **134**, 559 (2004).
23. E. Kim, M. H. W. Chan, *Phys. Rev. Lett.* **97**, 115302 (2006).
24. H. Choi, S. Kwon, D. Y. Kim, E. Kim, *Nat. Phys.* **6**, 424 (2010).

25. Supported by the National Research Foundation of Korea through Creative Research Initiatives and the Japan Society for the Promotion of Science through a Grant-in-Aid for Scientific Research. We thank members of the Center for Supersolid and Quantum Matter Research, in particular D. Y. Kim and S. Kwon, for helpful discussions.

12 August 2010; accepted 8 November 2010
Published online 18 November 2010;
10.1126/science.1196409

In Situ Observation of the Electrochemical Lithiation of a Single SnO_2 Nanowire Electrode

Jian Yu Huang,[1]* Li Zhong,[2] Chong Min Wang,[3]* John P. Sullivan,[1]* Wu Xu,[4] Li Qiang Zhang,[2] Scott X. Mao,[2]* Nicholas S. Hudak,[1] Xiao Hua Liu,[1] Arunkumar Subramanian,[1] Hongyou Fan,[5] Liang Qi,[6,7] Akihiro Kushima,[7] Ju Li[6,7]*

We report the creation of a nanoscale electrochemical device inside a transmission electron microscope—consisting of a single tin dioxide (SnO_2) nanowire anode, an ionic liquid electrolyte, and a bulk lithium cobalt dioxide ($LiCoO_2$) cathode—and the in situ observation of the lithiation of the SnO_2 nanowire during electrochemical charging. Upon charging, a reaction front propagated progressively along the nanowire, causing the nanowire to swell, elongate, and spiral. The reaction front is a "Medusa zone" containing a high density of mobile dislocations, which are continuously nucleated and absorbed at the moving front. This dislocation cloud indicates large in-plane misfit stresses and is a structural precursor to electrochemically driven solid-state amorphization. Because lithiation-induced volume expansion, plasticity, and pulverization of electrode materials are the major mechanical effects that plague the performance and lifetime of high-capacity anodes in lithium-ion batteries, our observations provide important mechanistic insight for the design of advanced batteries.

Lithiation and delithiation of the electrode materials in lithium-ion batteries (LIBs) induce large strains in the host material, leading to plasticity and fracture. Lithiation is also often accompanied by phase transformations, such as electrochemically driven solid-state amorphization (ESA) (*1*). These electrochemical reaction–induced microstructural events limit the energy capacity and cycle lifetime of LIBs (*2*–*6*). It was recently reported that lithium-ion anode materials composed of nanowires (*7*–*12*) can offer improved performance and lifetime relative to those of micrometer-scale or larger materials. The improvements are often attributed to the nanowire's unique geometry and enhanced accommodation of the transformation strains that occur during cycling (*9*, *10*, *13*, *14*). However, the detailed mechanisms of strain-induced plasticity and strain accommodation in nanowires during electrochemical charging are largely unknown.

We have successfully constructed a nanoscale electrochemical device consisting of a single SnO_2 nanowire as an anode, an ionic liquid–based electrolyte (ILE), and a cathode of $LiCoO_2$ particles inside a high-resolution transmission electron microscope (HRTEM) (Fig. 1A) to enable direct real-time visualization of electrochemical reaction–induced microstructural changes. As shown in Fig. 1B, the initial SnO_2 nanowire was straight with a smooth surface morphology. After contact with the ILE, the ILE wicked up the nanowire, forming a meniscus (Fig. 1C). Potential was then applied to the SnO_2 nanowire at –3.5 V with respect to the $LiCoO_2$ counterelectrode. This initiated an electrochemical reaction at the point of contact between the SnO_2 nanowire and the ILE where reduction of the SnO_2 was observed. This solid-state reaction front propagated along the longitudinal direction of the nanowire away from the electrolyte (Fig. 1, D to S, and movie S1). As the reaction front propagated, the diameter and length of the nanowire increased, and the TEM image contrast changed from typical crystalline diffraction contrast to a gray, mostly featureless contrast typical of amorphous materials (Fig. 2 and Fig. 3). At 625 s (Fig. 1, I and P to S, and movie S1), the nanowire began to flex rapidly, which resulted in the formation of a bend and the start of a coil of a spiral. After 1860 s of charging, the initially straight nanowire (Fig. 1B) exhibited a twisted and meandering morphology (Fig. 1O), indicative of extensive plastic deformation and microstructural changes. It took about half an hour to charge a nanowire with initial length of 16 μm and diameter of 188 nm. After charging, this nanowire had elongated ~60%, the diameter expanded ~45%, and the total volume expanded about 240%.

[1]Center for Integrated Nanotechnologies, Sandia National Laboratories, Albuquerque, NM 87185, USA. [2]Department of Mechanical Engineering and Materials Science, University of Pittsburgh, Pittsburgh, PA 15261, USA. [3]Environmental Molecular Sciences Laboratory, Pacific Northwest National Laboratory, Richland, WA 99354, USA. [4]Energy and Environment Directorate, Pacific Northwest National Laboratory, Richland, WA 99354, USA. [5]Advanced Materials Lab, Sandia National Laboratories, Albuquerque, NM 87106, USA. [6]State Key Laboratory for Mechanical Behavior of Materials and Frontier Institute of Science and Technology, Xi'an Jiaotong University, Xi'an 710049, China. [7]Department of Materials Science and Engineering, University of Pennsylvania, Philadelphia, PA 19104, USA.

*To whom correspondence should be addressed. E-mail: jhuang@sandia.gov (J.Y.H.); chongmin.wang@pnl.gov (C.M.W.); jpsulli@sandia.gov (J.P.S.); sxm2@pitt.edu (S.X.M.); liju@seas.upenn.edu (J.L.)

The large shape change of the nanowire during charging was a general feature of all the nanowires that were investigated. In fig. S1, A to K, we show the structural changes of another SnO_2 nanowire before and after charging, in this case polarized to −4 V with respect to the $LiCoO_2$ cathode. It took about 80 min to charge this nanowire with an initial length of 14 μm and diameter of 107 nm. After charging, the initially straight nanowire became highly distorted, with a total elongation of 90%, a diameter expansion of 35%, and a total volume expansion of 250%. Figure S2 shows the charging dynamics of a third nanowire. Large shape changes were observed again.

Figure 2 shows a more detailed structure and phase characterization of the nanowire before and after charging. Close inspection of the reaction front (Fig. 2A) revealed the presence of a region of a high density of dislocations separating the nonreacted and reacted segments of the nanowire. Before reaction, the nanowire was straight and monocrystalline, as revealed by the electron diffraction pattern (EDP) (Fig. 2B). Immediately after charging, the nanowire showed a dark gray contrast (Fig. 2A), and the EDP of most areas showed amorphous haloes (Fig. 2D). After prolonged charging, the nanowire comprised small nanocrystals dispersed in an amorphous matrix (Fig. 2F), and the EDP showed diffraction rings superimposed on diffuse amorphous haloes (Fig. 2E); the diffraction rings could be indexed as hexagonal Li_xSn (orange indices in Fig. 2E) and tetragonal Sn (black indices in Fig. 2E). The EDP from the reaction front (Fig. 2C) showed diffraction spots superimposed on a diffuse scattering background. These diffraction spots are similar to that of the nonreacted nanowire, except that the zone axis of the former is slightly tilted with respect to the latter. Electron energy loss spectroscopy (EELS) indicated that, after reaction, the nanowire contained metallic Sn, Li, and Li_2O (Fig. 2, G and H). EELS from a charged segment of the nanowire, such as that shown in Fig. 2A, showed the presence of Li (Fig. 2G, red line profile). The Li-K edge is similar to that of Li_2O rather than metallic Li (*15*), indicating that the amorphous phase is Li_2O. Occasionally, an EDP revealed the presence of nanocrystalline Li_2O, which was found in the nanowire after charging (fig. S3). These results revealed that the nanowire after charging consists of nanocrystalline Li_xSn and Sn particles dispersed in an amorphous Li_2O matrix.

In total, these measurements reveal that when a SnO_2 nanowire was polarized at a sufficiently negative potential with respect to $LiCoO_2$, the SnO_2 was initially reduced to nanocrystalline Sn

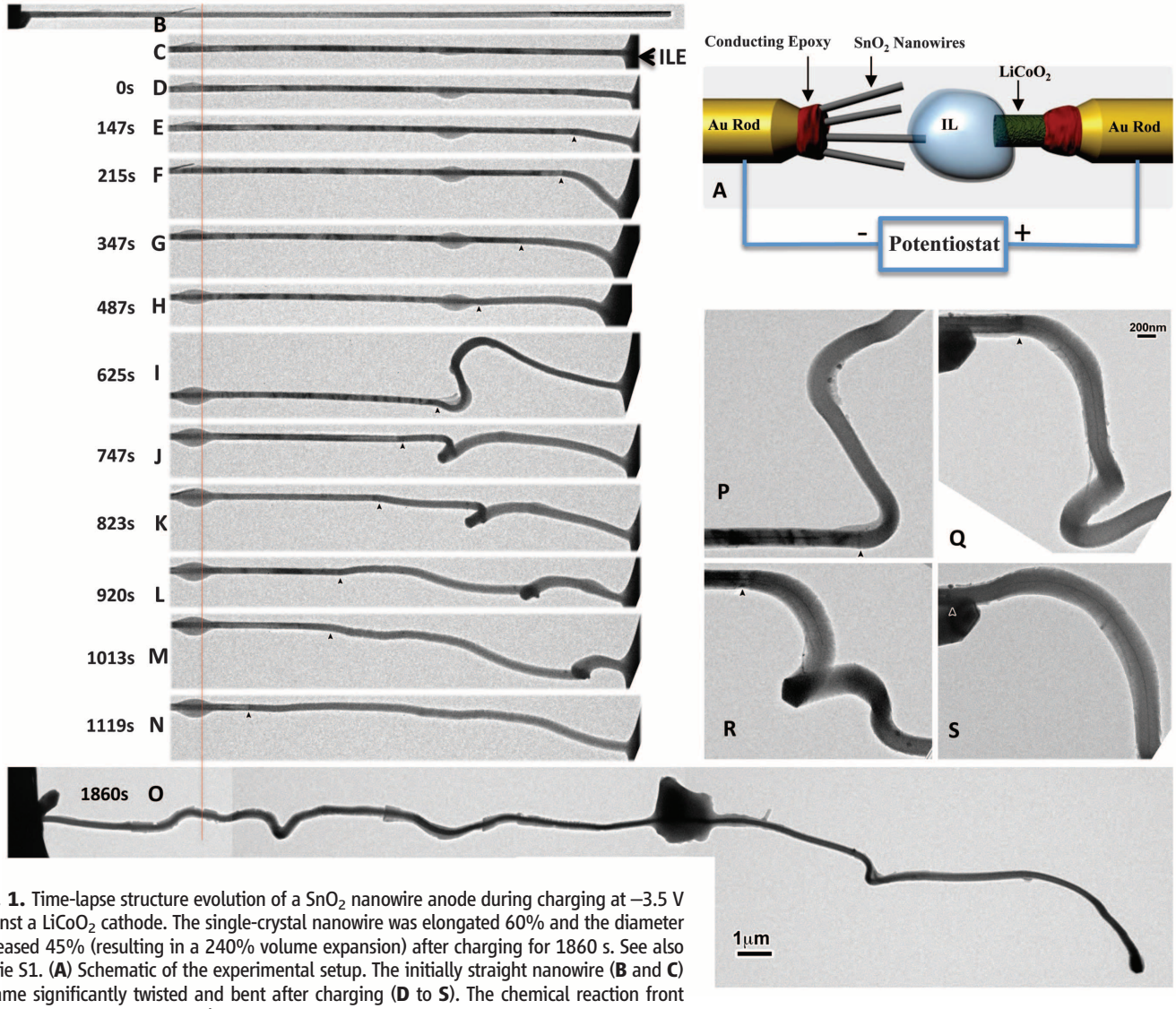

Fig. 1. Time-lapse structure evolution of a SnO_2 nanowire anode during charging at −3.5 V against a $LiCoO_2$ cathode. The single-crystal nanowire was elongated 60% and the diameter increased 45% (resulting in a 240% volume expansion) after charging for 1860 s. See also movie S1. (**A**) Schematic of the experimental setup. The initially straight nanowire (**B** and **C**) became significantly twisted and bent after charging (**D** to **S**). The chemical reaction front progressed along the nanowire's longitudinal direction, with the front clearly visible, as pointed out by arrowheads in (E) to (S). The red line in (B) to (O) marks a reference point to track the change of the nanowire length. (P) to (S) are sequential high-magnification images showing the progressive migration of the reaction front, swelling, and the twisted morphology of the nanowire after the reaction front passed by. The big dark particle in the middle of (O) is an island of gelled ILE. Because of the long cumulative electron beam exposure time during the recording of TEM images, the ILE front became gelled (with high viscosity) at this spot.

and amorphous Li_2O, which suggests the following reduction reaction: $4Li^+ + SnO_2 + 4e^- \rightarrow 2Li_2O + Sn$. This is the "forming stage" to produce a Sn-containing anode. After this initial phase transformation, the operation of the Sn-$LiCoO_2$ battery is based on a reversible reaction, such as $Sn + x\,Li^+ + x\,e^- \leftrightarrow Li_xSn$ ($0 \le x \le 4.4$) (*16*). While reduction was occurring at the SnO_2 nanowire anode, at the $LiCoO_2$ cathode Co was being oxidized from Co^{3+} to Co^{4+}, and Li^+ ions were expelled; that is, $LiCoO_2 \rightarrow Li_{1-\delta}CoO_2 + \delta\,Li^+ + \delta\,e^-$.

In contrast to bulk SnO_2, which is a brittle ceramic, nanowire SnO_2 showed large plasticity (as evidenced by the high dislocation density at the reaction front), and we did not observe fracture or cracking despite the high strain at the reacting interface. Details of the generation and migration of the dislocations near the reacting interface are shown in Fig. 3 and movies S2 to S5. In SnO_2, the width of this region of high dislocation density was ~10^2 nm, and is named the "Medusa zone" because of the appearance of dislocations "snaking" away from the interface. It may occur in certain electrochemical solid-state reactions, and its existence indicates very high stresses at the reaction front; the high stress drives dislocation nucleation and motion. Previously, ex situ TEM studies showed that a high density of dislocations may exist in $LiCoO_2$ cathodes in LIBs as a result of electrochemical cycling (*17*). However, it is far from clear when and how these dislocations are generated and how they evolve during cycling. Our in situ movies show that the dislocations were continuously nucleated in the crystal regions and then moved away from the highly stressed region. They were also pursued from behind and absorbed by the moving amorphous-crystalline interface (ACI) (*18*), thereby maintaining a steady state in the total dislocation cloud, which migrated in an approximate chevron shape along the nanowire. One type of dislocation in SnO_2 is determined to be of $[01\bar{1}](100)$ slip character (fig. S4). We have performed ab initio density functional theory (DFT) calculations and found the ideal shear strength of SnO_2 to be ~10 GPa. Because a very high density of dislocations was seen to be nucleated readily and continuously at the interface even as the old nucleation zone was being demolished by the advancing reaction front (which would imply the removal of the original Frank-Read dislocation sources), we postulate that

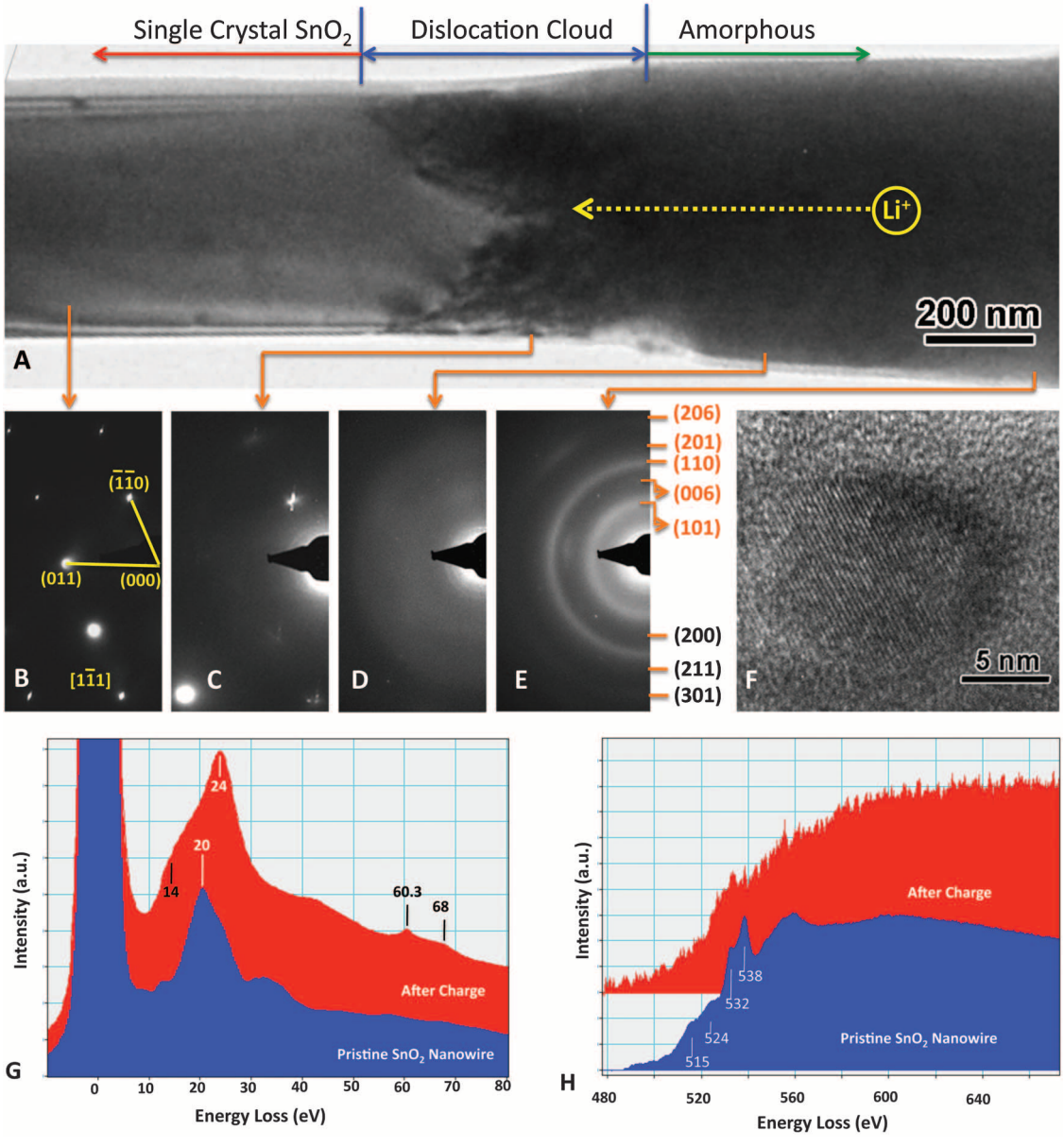

Fig. 2. Structural and phase characterization of another SnO_2 nanowire anode during charging at −3.5 V against the $LiCoO_2$ cathode. (**A**) TEM micrograph of the nanowire containing a reaction front ("dislocation cloud") separating the reacted ("amorphous") and nonreacted ("single-crystal SnO_2") sections. (**B** to **E**) EDPs from the different sections of the nanowire. The pristine nanowire was single crystalline and the corresponding EDP (B) can be indexed as the $[1\bar{1}1]$ zone axis of rutile SnO_2. The EDP from the dislocation zone (C) shows a spot pattern superimposed on a diffuse scattering background. The EDP from an area immediately after the reaction front (D) shows an amorphous halo. The EDP from an area far away from the reaction front (E) shows diffraction rings superimposed on a diffuse amorphous halo. The diffraction rings can be indexed as tetragonal Sn (black indices) and a Li_xSn compound such as hexagonal $Li_{13}Sn_5$ (orange indices). (**F**) A HRTEM image from a charged nanowire showing Sn nanoparticles dispersed in an amorphous matrix. (**G** to **H**) Low-loss and core-loss EELS from a large area of the nanowire after reaction (red line profile) and a pristine nanowire (blue line profile). The pristine SnO_2 shows two characteristic core-loss peaks at 515 and 524 eV, corresponding to the Sn-$M_{4,5}$ edge riding on a delayed edge. The peaks at 532 and 538 eV arise from the O-K edge. Note that Li is present in the charged nanowire (G). The plasmon loss peaks at 20 eV, 24 eV, and 14 eV are in excellent agreement with SnO_2, Li_2O, and pure Sn, respectively.

a stress close to the ideal strength (*14*) should exist in the Medusa zone. Such a large stress would be expected at the reaction interface, as the reacted side of the interface exhibits a 45% increase in radial expansion relative to the unreacted side. This would generate a large tensile stress near the ACI that leads to spontaneous dislocation nucleation on the unreacted side, and a large compressive stress on the reacted amorphous side. Plasticity is expected to also occur on the amorphous side (*18*, *19*), despite the lack of dislocations.

We note two important consequences of the observed dislocation structure and dynamics at the reacting interface. First, the dislocation cores may be highly effective Li transport channels (*20*) and may facilitate Li ion insertion into the crystalline interior, effectively increasing the reaction kinetics. Second, the amorphous phase we observed in situ did not form via the melt-quench mechanism, but via a direct crystal-to-glass transition (i.e., ESA) (*1*). Solid-state amorphization (*21*–*23*) has often been associated with mechanical alloying of bulk materials (e.g., ball-milling) (*24*–*26*). Here it is observed in the context of an electrochemical reaction with large stress and apparent dislocation plasticity at the reaction front. Fortunately, electron transparency allows us to capture the dynamical process of ESA with TEM. Our observations suggest that stress-driven dislocation plasticity may be a precursor to some solid-state amorphizations (*23*–*26*). The dislocation density we observed in the Medusa zone was exceptionally high, on the order of $10^{17}/m^2$, which is about two orders of magnitude larger than that in heavily work-hardened face-centered cubic metals (*27*). Such a high dislocation density was caused by the exceptionally high stress driven by the electrochemical reaction. The dislocation cloud disturbs the structural order of the crystal and drives it far from equilibrium. This can provide the necessary energy and kinetic pathway toward complete amorphization.

In addition to the interesting precipitate/dislocation microstructures, we observed very unusual gross morphological changes of the nanowire. Elastic energy strongly influences the shape of phase transformation products (*28*), and the nanowire geometry provides an elasticity boundary condition very different from that of 3D bulk materials. For the SnO_2 nanowire polarized at –4 V versus $LiCoO_2$ (fig. S1), we observed a very large anisotropy in the transformation strain, namely ~90% elongation in the ⟨011⟩ axial direction compared to ~35% expansion in the transverse directions; the total volume expanded by ~250%. Our DFT calculation gives a net volume expansion that matches very well with the experimental result (table S1), assuming $x = 3$ in the charging reaction $(4 + x)Li^+ + SnO_2 + (4 + x)e^- \rightarrow 2Li_2O + Li_xSn$. But the calculated transformation strain anisotropy, based on uniform electrochemical Li^+ insertions alone, is completely different; that is, the largest expansion should occur along ⟨001⟩ instead of ⟨011⟩. We interpret this contrast as due to the buckling instability of the nanowire (movie S1); the wire is elastically very compliant in the axial direction and therefore prefers to accommodate the volume expansion in the axial direction. In the transverse directions, because of geometric con-

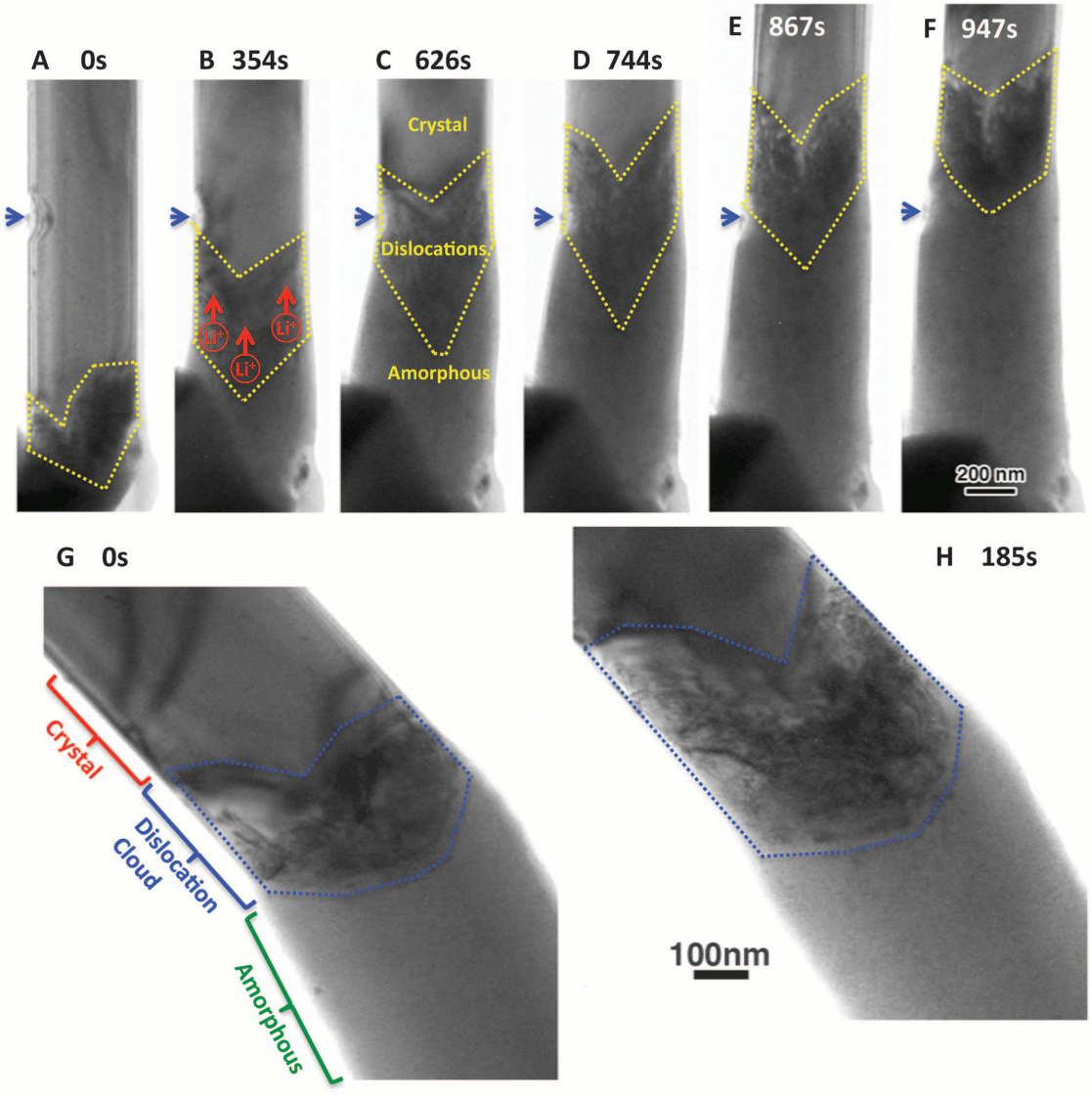

Fig. 3. TEM images revealed a high density of dislocations emerging from the reaction front (marked by chevron-shaped dotted lines). As the dislocation front propagated, the crystalline contrast changed to gray amorphous contrast instantaneously, and the nanowire diameter increased immediately. See also movies S2 to S5. (**A** to **F**) and (**G** and **H**) Two sets of time-lapsed TEM images showing the high density of dislocations that appeared at the reaction front and the migration of the reaction front.

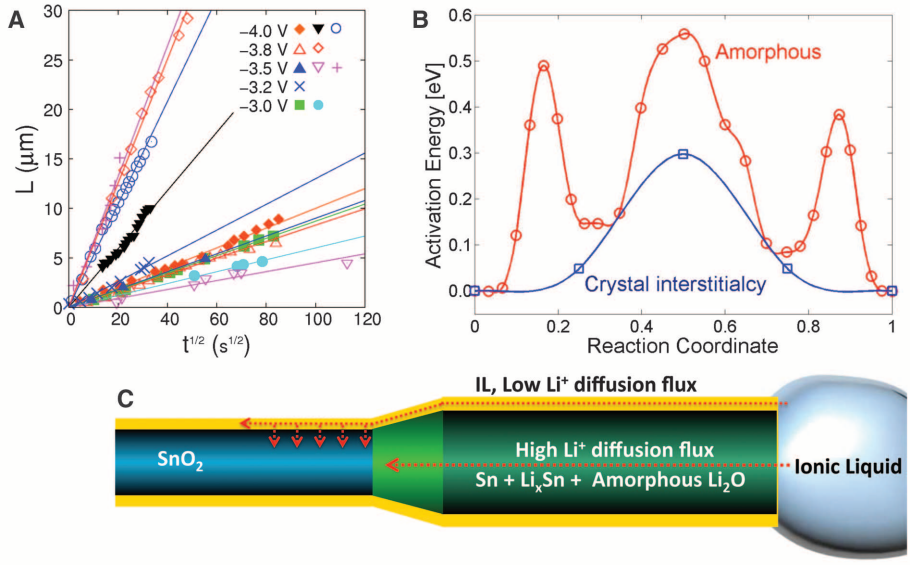

Fig. 4. (**A**) Plot of the reaction front migration distance *L* versus the square root of time for 11 nanowires. (**B**) Representative Li^+ migration energy barrier in crystalline and amorphous Li_2O from DFT calculations. (**C**) Schematic drawing showing the high Li diffusion flux in Li_2O.

straints at the ACI, large in-plane stresses develop that drive mechanical plasticity. The net shape change of the nanowire observed is therefore not due to lithiation alone, but is the combined outcome of electrochemical-mechanical actions, where stress-induced plasticity plays an important part (fig. S5). These shape-change features mean that the design and packaging of nanowire nanobatteries must take into account the large conformation changes of the nanowire (buckling, coiling, and twisting) without breaking electrical contact or shorting across electrodes. It is also noteworthy that among the several nanowires we charged and discharged, none of them fractured despite the large strain and conformational changes. This is further testimony to the mechanical robustness associated with the nanowire geometry relative to bulk ceramic electrodes (*13*, *14*).

The displacement of the reaction front versus the square root of reaction time is plotted in Fig. 4A using the results of 11 experiments. The nearly parabolic behavior indicates the importance of long-range Li^+ diffusion (Fig. 4C). On the basis of our data, the diffusivity of Li^+ in the reacted amorphous sections ranges from 5×10^{-16} to 5×10^{-14} m^2/s, which is of the same range as the results reported for bulk Li_2O (*29*–*31*) if extrapolated to room temperature. The somewhat large scattering in diffusivity value is reasonable, because unlike a crystal, the amorphous atomic structure is not unique, and slightly different formation conditions (for example, due to different local voltage) of the amorphized nanowire can lead to different diffusivities. The characteristic migration energy barrier of ~0.4 eV (Fig. 4B), obtained from our ab initio calculations using an ensemble of Li^+ migration paths in Li_2O with approximately the same initial and final potential energies, matches our experimental diffusivities reasonably well. Note that the wetting layer of ILE on the nanowire surface is so thin (less than 10 nm) that the flux of Li^+ transported by this layer is outmatched by the flux from solid-state diffusion in the amorphous Li_2O reaction product. This explains why the reaction occurred along the longitudinal direction rather than along the radial direction.

To imitate the scenario in a real battery configuration, we have also conducted experiments with the nanowire partially immersed in the ILE to see whether there is any difference in the post-charging shape changes between the immersed segments and the exposed segments of the nanowire (fig. S6). We found no essential difference in the final shape between the two different segments of the nanowire, both of which show large shape changes with extensive buckling and spiraling (fig. S6).

After charging, we also performed discharge, and TEM showed that the Li_xSn alloy nanoparticles were converted back to pure Sn (fig. S7) and that the diameter of the nanowire decreased. The overall volume change during discharge was much less than during the initial charging process, however. During initial charging, the formation of Li_2O caused large volume expansion [irreversible (*16*)], whereas in the discharging process, the Li_2O glass did not participate in the electrochemical reaction and only the Li_xSn nanoprecipitates, which occupy smaller volume, were active. Although the successful charging and discharging demonstrate that this system constitutes a working electrochemical device (*32*), we were unable to quantify the reversible capacity of this device because the low discharge current (estimated to be less than 3 pA) was much lower than our noise floor for our electrical current measurement.

The methodology described above should stimulate real-time studies of the microscopic processes in batteries and lead to a more complete understanding of the mechanisms governing battery performance and reliability, especially those properties that are controlled by microstructure. Although the work was carried out using SnO_2 nanowires, these experiments can be extended to other materials, for either cathode or anode studies. Further, autonomous nanomachines such as nanorobots (*33*) call for extreme miniaturization of power supplies (*34*) with energy generation (*35*) and energy storage functions. The concept of a stand-alone rechargeable nanobattery that uses individual nanowires as electrodes and a nanoscale electrolyte is quite appealing. Although our work falls short of realizing a fully packaged nanobattery, we believe that the in situ characterization and modeling reported here is an important step toward achieving that goal.

References and Notes

1. P. Limthongkul, Y. I. Jang, N. J. Dudney, Y. M. Chiang, *Acta Mater.* **51**, 1103 (2003).
2. A. K. Padhi, K. S. Nanjundaswamy, J. B. Goodenough, *J. Electrochem. Soc.* **144**, 1188 (1997).
3. J. M. Tarascon, M. Armand, *Nature* **414**, 359 (2001).
4. Y. Shao-Horn, L. Croguennec, C. Delmas, E. C. Nelson, M. A. O'Keefe, *Nat. Mater.* **2**, 464 (2003).
5. B. Kang, G. Ceder, *Nature* **458**, 190 (2009).
6. W. Lai *et al.*, *Adv. Mater.* **22**, E139 (2010).
7. K. T. Nam *et al.*, *Science* **312**, 885 (2006); 10.1126/science.1122716.
8. M. S. Park *et al.*, *Angew. Chem. Int. Ed.* **46**, 750 (2007).
9. C. K. Chan *et al.*, *Nat. Nanotechnol.* **3**, 31 (2008).
10. H. Kim, J. Cho, *Nano Lett.* **8**, 3688 (2008).
11. Y. D. Ko, J. G. Kang, J. G. Park, S. Lee, D. W. Kim, *Nanotechnology* **20**, 455701 (2009).
12. A. Magasinski *et al.*, *Nat. Mater.* **9**, 353 (2010).
13. T. K. Bhandakkar, H. J. Gao, *Int. J. Solids Struct.* **47**, 1424 (2010).
14. T. Zhu, J. Li, *Prog. Mater. Sci.* **55**, 710 (2010).
15. D. R. Liu, D. B. Williams, *Philos. Mag. B* **53**, L123 (1986).
16. I. A. Courtney, J. R. Dahn, *J. Electrochem. Soc.* **144**, 2045 (1997).
17. H. Gabrisch, R. Yazami, B. Fultz, *Electrochem. Solid State Lett.* **5**, A111 (2002).
18. Y. M. Wang, J. Li, A. V. Hamza, T. W. Barbee Jr., *Proc. Natl. Acad. Sci. U.S.A.* **104**, 11155 (2007).
19. Z. W. Shan *et al.*, *Phys. Rev. B* **77**, 155419 (2008).
20. M. Legros, G. Dehm, E. Arzt, T. J. Balk, *Science* **319**, 1646 (2008).
21. D. Wolf, P. R. Okamoto, S. Yip, J. F. Lutsko, M. Kluge, *J. Mater. Res.* **5**, 286 (1990).
22. H. J. Fecht, *Nature* **356**, 133 (1992).
23. H. Bakker, G. F. Zhou, H. Yang, *Prog. Mater. Sci.* **39**, 159 (1995).
24. C. Suryanarayana, *Prog. Mater. Sci.* **46**, 1 (2001).
25. J. Y. Huang, H. Yasuda, H. Mori, *Philos. Mag. Lett.* **79**, 305 (1999).
26. J. Y. Huang, Y. T. Zhu, X. Z. Liao, R. Z. Valiev, *Philos. Mag. Lett.* **84**, 183 (2004).
27. H. Mughrabi, *Philos. Mag.* **86**, 4037 (2006).
28. A. G. Khachaturyan, *Theory of Structural Transformations in Solids* (Wiley, New York, 1983).
29. H. Ohno *et al.*, *J. Nucl. Mater.* **118**, 242 (1983).
30. T. Oda, S. Tanaka, *J. Nucl. Mater.* **386–388**, 1087 (2009).
31. J. Habasaki, Y. Hiwatari, *Phys. Rev. B* **69**, 144207 (2004).
32. A. Brazier *et al.*, *Chem. Mater.* **20**, 2352 (2008).
33. K. Kostarelos, *Nanomedicine* **5**, 341 (2010).
34. A. E. Curtright, P. J. Bouwman, R. C. Wartena, K. E. Swider-Lyons, *Int. J. Nanotechnol.* **1**, 226 (2004).
35. Z. L. Wang, J. Song, *Science* **312**, 242 (2006).

36. J.Y.H. thanks K. Xu for valuable discussions. Supported by a Laboratory Directed Research and Development (LDRD) project at Sandia National Laboratories (SNL) and by the Science of Precision Multifunctional Nanostructures for Electrical Energy Storage (NEES), an Energy Frontier Research

Center funded by the U.S. Department of Energy (DOE), Office of Science, Office of Basic Energy Sciences (BES) under award DESC0001160. This work was performed in part at the Sandia-Los Alamos Center for Integrated Nanotechnologies (CINT), a U.S. DOE, Office of BES user facility. The LDRD supported the development and fabrication of platforms and the development of TEM techniques. The NEES center supported some of the additional platform development and fabrication and materials characterization. CINT supported the TEM capability and the fabrication capabilities that were used for the TEM characterization, and this work represents the efforts of several CINT users, primarily those with affiliation external to SNL. SNL is a multiprogram laboratory operated by Sandia Corporation, a wholly owned subsidiary of Lockheed Martin company, for the DOE's National Nuclear Security Administration under contract DE-AC04-94AL85000. The work of C.M.W. and W.X. was supported by the DOE Office of Science, Offices of Biological and Environmental Research, and was conducted in the Environmental Molecular Sciences Laboratory, a national scientific user facility sponsored by DOE's Office of Biological and Environmental Research and located at Pacific Northwest National Laboratory, which is operated by Battelle for the DOE under contract DE-AC05-76RLO1830. L.Q., A.K., and J.L. were supported by Honda Research Institute USA, Xi'an Jiaotong University, NSF grants CMMI-0728069, DMR-1008104, and DMR-0520020, and Air Force Office of Scientific Research grant FA9550-08-1-0325. S.X.M., L.Z., and L.Q.Z. were supported by NSF grants CMMI0825842 and CMMI0928517 through the University of Pittsburgh and SNL. L.Q.Z. thanks the Chinese Scholarship Council for financial support and Z. Ye's encouragement from Zhejiang University.

Supporting Online Material
www.sciencemag.org/cgi/content/full/330/6010/1515/DC1
Materials and Methods
Figs. S1 to S11
Movies S1 to S5
References

26 July 2010; accepted 26 October 2010
10.1126/science.1195628

Optomechanically Induced Transparency

Stefan Weis,[1,2]* Rémi Rivière,[2]* Samuel Deléglise,[1,2]* Emanuel Gavartin,[1] Olivier Arcizet,[3] Albert Schliesser,[1,2] Tobias J. Kippenberg[1,2]†

Electromagnetically induced transparency is a quantum interference effect observed in atoms and molecules, in which the optical response of an atomic medium is controlled by an electromagnetic field. We demonstrated a form of induced transparency enabled by radiation-pressure coupling of an optical and a mechanical mode. A control optical beam tuned to a sideband transition of a micro-optomechanical system leads to destructive interference for the excitation of an intracavity probe field, inducing a tunable transparency window for the probe beam. Optomechanically induced transparency may be used for slowing and on-chip storage of light pulses via microfabricated optomechanical arrays.

Coherent interaction of laser radiation with multilevel atoms and molecules can lead to quantum interference in the electronic excitation pathways (*1*). A prominent example observed in atomic three-level systems is the phenomenon of electromagnetically induced transparency (EIT), in which a control laser induces a narrow spectral transparency window for a weak probe laser beam. When this generic EIT effect had first been observed in an atomic gas (*2*), its relevance in nonlinear optics and optical (quantum) information processing was quickly recognized. In particular, the rapid variation of the refractive index concomitant with the opening of the transparency window gives rise to a dramatic reduction of the group velocity of a propagating optical pulse (*3*, *4*). Dynamic control of EIT with the control laser enables even a complete stop, that is, storage, of the pulse in an atomic medium (*5*, *6*). The experimental demonstration of slowing and stopping light (*3*–*6*) has attracted strong attention, because it provides a route to implement a photonic quantum memory (*7*) or a classical optical buffer. EIT has subsequently been studied in a wide variety of atomic media, but also in several solid-state systems (*8*, *9*) with a well-suited level structure.

Recent experiments with optomechanical systems have demonstrated that the mechanical response to thermal forces can be controlled by an optical field. This effect has been exploited, for example, to implement optomechanical laser cooling and amplification (*10*–*13*) as well as normal mode splitting (*14*). In other work, the mechanical response was optically tailored to exhibit destructive interference between different mechanical excitation pathways (*15*). Whereas in these studies, the mechanical response to thermal Langevin force was modified, we demonstrate here, as recently suggested (*16*, *17*), that the system's optical response to a weak "probe" laser can be controlled by a second "control" laser driving the lower motional sideband. A window of transparency arises from the destructive interference of excitation pathways for the intracavity probe field when a two-photon resonance condition is met. As pointed out independently, this effect can be considered a strict optomechanical analog of EIT (*18*), originating from a similar effective interaction Hamiltonian (*19*). Advantageously, this form of induced transparency does not rely on naturally occurring resonances and could therefore also be applied to previously inaccessible wavelength regions such as the technologically important near-infrared. Furthermore, a single optomechanical element can already achieve unity contrast, which in the atomic case is only possible within the setting of cavity quantum electrodynamics (*20*).

Our experiment (Fig. 1) consists of an optomechanical system featuring linear optomechanical coupling G in the sense that the cavity resonance frequency is given by $\omega_c'(x) = \omega_c + Gx$, where ω_c is the unperturbed resonance frequency. A control laser (frequency ω_l) maintains a control field $\bar{a}e^{-i\omega_l t}$, containing $|\bar{a}|^2$ photons, in the cavity. The static radiation pressure originating from this field displaces the mechanical mode by $\bar{x}$, leading to an effective detuning from the cavity resonance $\bar{\Delta} = \omega_l - (\omega_c + G\bar{x})$. We consider the situation where the control laser is tuned close to the lower motional sideband, i.e., $\bar{\Delta} \approx -\Omega_m$, where Ω_m is the mechanical (angular) resonance frequency. A second, weak laser oscillating at $\omega_p = \omega_l + \Omega$, is subsequently used to probe the (modified) cavity resonance by driving an intracavity probe field contained in a perturbation term $\delta a(t)$.

In the case of a weak probe field (compared to the control field), one can linearize the optomechanical dynamics (*21*) for the mechanical displacement $x(t) = \bar{x} + \delta x(t)$ and the intracavity field $a(t) = [\bar{a} + \delta a(t)]e^{-i\omega_l t}$ around the steady-state values $(\bar{x}, \bar{a})$. For the probe power transmission—that is, the ratio of the probe power returned from the system divided by the input probe power—the general expression

$$|t_p|^2 = \left| 1 - \frac{1 + if(\Omega)}{-i(\bar{\Delta} + \Omega) + \kappa/2 + 2\bar{\Delta}f(\Omega)} \eta_c \kappa \right|^2 \quad (1)$$

with

$$f(\Omega) = \hbar G^2 \bar{a}^2 \; \frac{\chi(\Omega)}{i(\bar{\Delta} - \Omega) + \kappa/2} \quad (2)$$

can be derived [see (*16*–*18*) and supporting online material (SOM) Eq. S25]. Here, $\chi(\Omega) = [m_{\mathrm{eff}}(\Omega_m^2 - \Omega^2 - i\Gamma_m\Omega)]^{-1}$ is the susceptibility of the mechanical oscillator of effective mass m_{eff} and damping rate Γ_m. The optical mode is characterized by a total loss rate $\kappa = \kappa_0 + \kappa_{ex}$ and the cavity coupling parameter $\eta_c = \kappa_{ex}/(\kappa_0 + \kappa_{ex})$. The presence of a control field $\bar{a}$ (tuned to the lower sideband) induces a transmission window for the probe beam when the resonance condition $\Omega \approx \Omega_m$ is met (Fig. 1). The depth and the width of this transmission window are tunable by the power of the control beam, as in the case of atomic EIT, with the best contrast achieved in the case of critical coupling $\eta_c = 1/2$.

To gain more physical insight into this phenomenon, it is instructive to consider this effect in a sideband picture. The simultaneous presence of control and probe fields generates a radiation-

[1]Ecole Polytechnique Fédérale de Lausanne, EPFL, 1015 Lausanne, Switzerland. [2]Max-Planck-Institut für Quantenoptik, Hans-Kopfermann-Strasse 1, 85748 Garching, Germany. [3]Institut Néél, 25 Rue des Martyrs, 38042 Grenoble, France.

*These authors contributed equally to this work.
†To whom correspondence should be addressed. E-mail: tobias.kippenberg@epfl.ch

Supporting Online Material for

In Situ Observation of the Electrochemical Lithiation of a Single SnO_2 Nanowire Electrode

Jian Yu Huang,* Li Zhong, Chong Min Wang,* John P. Sullivan,* Wu Xu, Li Qiang Zhang, Scott X. Mao,* Nicholas S. Hudak, Xiao Hua Liu, Arunkumar Subramanian, Hong You Fan, Liang Qi, Akihiro Kushima, Ju Li*

*To whom correspondence should be addressed. E-mail: jhuang@sandia.gov (J.Y.H.); chongmin.wang@pnl.gov (C.M.W.); jpsulli@sandia.gov (J.P.S.); sxm2@pitt.edu (S.X.M.); liju@seas.upenn.edu (J.L.)

Published 10 December 2010, *Science* **330**, 1515 (2010)
DOI: 10.1126/science.1195628

This PDF file includes:

Other supporting material for this manuscript includes the following:

Supporting Online Movies

Supporting online movies can also be downloaded from the following web server:
http://mt.seas.upenn.edu/Stuff/sn/Movie/

Movie S1. An in-situ TEM movie showing the microstructural evolution of a SnO_2 NW anode as it was charged at -3.5 V vs. $LiCoO_2$. As the reaction front passed by, the former SnO_2 nanowire's diameter expanded, and the length elongated. In the meantime, crystalline SnO_2 was converted to nanocrystalline Sn and Li_xSn dispersed in an amorphous Li_2O matrix. The video was recorded at 2 frame/s and played at 33×.
http://mt.seas.upenn.edu/Stuff/JianyuHuang/Upload/S1.mov

Movie S2. An in-situ TEM movie showing that dislocations are continuously emitted from the reaction front. As the reaction front or the high density of dislocations passed by, the crystalline contrast changed to a gray amorphous contrast, and the diameter and length of the nanowire increased. The video was recorded at 2 frame/s and played at 30×.
http://mt.seas.upenn.edu/Stuff/JianyuHuang/Upload/S2.mov

Movie S3. An in-situ TEM movie showing a high density of dislocations in the reaction front. As the reaction front or the high density of dislocations swept by, the crystalline contrast changed to a gray amorphous contrast, and the diameter and length of the nanowire were increased. The video was recorded at 2 frame/s and played at 50×.
http://mt.seas.upenn.edu/Stuff/JianyuHuang/Upload/S3.mov

Movie S4. An in-situ TEM movie showing that dislocations were continuously emitted from the reaction front. As the reaction front or the high density of dislocations advanced, the crystalline contrast changed to a gray amorphous contrast, and the diameter and length of the nanowire were increased. The video was recorded at 2 frame/s and played at 34×.
http://mt.seas.upenn.edu/Stuff/JianyuHuang/Upload/S4.mov

Movie S5. An in-situ TEM movie showing that dislocations were continuously emitted from the reaction front. As the reaction front or the high density of dislocations swept by, the crystalline contrast changed to a gray amorphous contrast, and the diameter and length of the nanowire were increased. The video was recorded at 2 frame/s and played at 50×.
http://mt.seas.upenn.edu/Stuff/JianyuHuang/Upload/S5.mov

Supporting Online Materials:

In situ observation of the electrochemical lithiation of a single SnO_2 nanowire electrode

Jian Yu Huang,[1*] Li Zhong,[2] Chong Min Wang,[3*] John P. Sullivan,[1*] Wu Xu,[4] Li Qiang Zhang,[2] Scott X. Mao,[2*] Nicholas S. Hudak,[1] Xiao Hua Liu,[1] Arunkumar Subramanian,[1] Hong You Fan,[5] Liang Qi,[6,7] Akihiro Kushima,[6] Ju Li[6,7*]

[1]Center for Integrated Nanotechnologies, Sandia National Laboratories, Albuquerque, New Mexico 87185, USA
[2]Department of Mechanical Engineering and Materials Science, University of Pittsburgh, Pittsburgh, Pennsylvania 15261, USA
[3]Environmental Molecular Sciences Laboratory, Pacific Northwest National Laboratory, Richland, Washington 99354, USA
[4]Energy and Environment Directorate, Pacific Northwest National Laboratory, Richland, Washington 99354, USA
[5]Advanced Materials Lab, Sandia National Laboratories, Albuquerque, New Mexico 87106, USA
[6]State Key Laboratory for Mechanical Behavior of Materials and Frontier Institute of Science and Technology, Xi'an Jiaotong University, Xi'an, 710049, China
[7]Department of Materials Science and Engineering, University of Pennsylvania, Philadelphia, Pennsylvania 19104, USA

Table of Contents

3. **Fig. S2.** In-situ time-lapsed TEM images of the charging process of a single SnO_2 nanowire negative electrode during charging at -3 V versus a $LiCoO_2$ cathode.

4. **Fig. S3.** Electron diffraction pattern (EDP) showing that nanocrystalline Li_2O and nanocrystalline Sn was occasionally observed in the nanowire after the charging reaction.

5. **Fig. S4.** A HRTEM image showing one type of dislocation generated in the reaction front.

6. **Fig. S5.** Nanowire shape change due to coupled electrochemical-mechanical actions.

7. **Fig. S6** Morphology changes of a SnO_2 nanowire after charging for 195 minutes at a potential of -3.5 V against $LiCoO_2$ cathode.

8. **Fig. S7.** TEM images of a charged "SnO_2" NW before and after discharge.

9. **Fig. S8** SEM images (A-C) showing the nanowire cross-section and HRTEM (D) showing the nanowire growth direction.

10. **Fig. S9** A SnO_2 nanowire with a Au core.

11. **Fig. S10.** Relaxed shear stress-strain response of crystalline SnO_2 on the (101) plane along the [-101] shear displacement direction, calculated with DFT.

12. **Fig. S11.** Mean squared displacement of Li atoms in *ab initio* MD simulation of $Li_{17}O_8$ super cell at 1200 K.

13. **Supporting References**

1. **Materials and Methods**

a. Construction of the nanowire battery

Transmission electron microscopy (TEM) observations were conducted in a Tecnai F30 microscope fitted with a Nanofactory™ TEM-scanning tunneling microscopy (STM) probe for *in-situ* nanowire manipulation. To create the test cell, an individual SnO_2 nanowire was attached to a gold rod, which was further attached to a piezo manipulator. Prior to insertion into the TEM, a drop of ILE [lithium bis (trifluoromethylsulfonyl) imide (LiTFSI) dissolved in 1-butyl-1-methylpyrrolidinium bis (trifluoromethylsulfonyl) imide (P_{14}TFSI)] was placed on the $LiCoO_2$ cathode surface. The ionic liquid is a molten organic salt with very low vapor pressure, enabling its use in the high vacuum (~10^{-5} Pa) inside the HRTEM while still solvating and transporting Li ions effectively. After loading the battery components into the TEM, an individual SnO_2 nanowire was manipulated in-situ and partially inserted into the ILE droplet, completing the assembly of the three critical components of the battery (anode, electrolyte, and cathode) (Fig. 1A). When assembled in this manner, the battery is in its discharged state (i.e. with lithium residing in the positive electrode, or cathode). The nanowire battery was charged by performing potentiostatic holds at different voltages (up to -4V) with respect to the $LiCoO_2$ cathode. These potentials were chosen because the open circuit voltage of SnO_2 vs. $LiCoO_2$ is about -2.9 V (*S1, S2*).

To minimize the effect of the electron beam impinging on the sample, the beam was "blanked" during the charging process except for very short exposures (~1s) about every five minutes for the purpose of recording images. However, when we needed to record a video, the beam was not blanked. We found no significant mechanistic differences between time lapse imaging with beam blanking and continuous imaging without blanking. In either case, an extremely low electron beam dose (~10^{-3} A/cm^2) was used to minimize beam damage artifacts.

b. SnO_2 nanowire preparation procedure

The SnO_2 nanowire was synthesized by a chemical vapor deposition (CVD) process using activated carbon powder (Ketjen Black, EC600JD, Akzo Nobel Corp. Japan) and SnO_2 nanoparticles (from Aldrich, particle size < 100 nm) as the precursors and Au as the catalyst. Details of the synthesis process were described in the published literature (*S3, S4*). We report a brief summary of the experimental procedure here. The activated carbon and the SnO_2 nanopowder were combined in a ratio of C:SnO_2 = 1:4 by weight and thoroughly dry mixed using a mortar and pestle. The mixed C and SnO_2 powder was placed into a quartz boat, which was subsequently loaded into a quartz tube furnace. A Si wafer, topped by a 5 nm thick sputter coated Au film, was located next to the quartz boat for the purpose of catalyzing the formation of the SnO_2 nanowires. The carrier gas was high purity nitrogen (99.95%) and was flowing in the direction from the mixed powder precursor towards the Si substrate. The nitrogen flow rate was 100 sccm with the pressure in the tube maintained at 200 Torr. The furnace was heated at a rate of 6.5 °C/min to 800 °C and maintained at 800 °C for 6 hours for the growth of the SnO_2 nanowires. Upon completion of the growth, the furnace power was shut off to allow the furnace to cool naturally. Typically, it took ~ 4 hours for the furnace to cool from 800 °C to room temperature. The diameter of the SnO_2

nanowires ranged from several nanometers to ~ 1 μm and the length of the wires ranged from several hundred nanometers to several hundred micrometers.

The cross-section of these nanowires is either polygonal, or hexagonal, or rhombic (see Fig. S8). The growth direction of the nanowires is [011] (Fig. S8). In some nanowires, a Au core was present (Fig. S9).

c.

Table S1. *Ab initio* density functional theory (DFT) calculated volume expansion for $x\mathrm{Li}^+ + x\mathrm{e}^-$ insertion into a SnO_2 crystal

x	Relative volume expansion
0	0
2	62%
4	149%
6	209%
8	270%

d. DFT Calculation Procedures

All the density functional theory (DFT) calculations were performed by using the Vienna *ab initio* simulation package (VASP) (*S5, S6*). We used projector augmented wave (PAW) potentials with the Perdew-Burke-Ernzerhof (PBE) exchange-correlation functional in non-spin-polarized condition (*S7, S8*). Monkhorst-Pack **k**-point grids for the Brillouin-zone integration were applied with **k**-point density higher than 18 per $Å^{-1}$ along each periodic direction in reciprocal space (*S9*). Partial occupancies of eigenstates were determined by a Gaussian smearing of $\sigma = 0.1$ eV. The cut-off energy for the plane wave basis was 400 eV.

The relaxed shear stress-strain relation of crystalline SnO_2 in rutile structure is calculated with VASP, and plotted in Fig. S10. To obtain reasonable volumes of amorphous Li_xSnO_2, we used VASP to do "simulated-annealing" in many cycles. The supercell of Li_xSnO_2 contains $2x$ Li atoms, 2 Sn atoms and 4 O atoms. In each cycle, *ab initio* molecular dynamic (MD) simulations were performed at extremely high temperature (3500 K) for 1000 time steps with step size of 0.2 fs. Then both the atomic structure and supercell volume were relaxed to a certain local minimum state, which would be the initial state for MD simulations in the next cycle. Final volume of amorphous Li_xSnO_2 was the average of the relaxation volume when they converged to certain stable values after tens of "simulated-annealing" cycles. The relative volume expansion is listed in Table S1.

To obtain the diffusivity of Li^+ inside the amorphous Li_2O matrix, minimum energy paths (MEPs) for the migration of Li^+ were searched in both crystalline and amorphous Li_2O by using the climbing image nudged elastic band (CI-NEB) method (*S10, S11*) in VASP, as shown in Fig. 4B. For crystalline Li_2O, a $2 \times 2 \times 2$ supercell was used so that the perfect lattice contains 32 Li atoms and 64 O atoms. Three different migration mechanisms (vacancy, interstitial and interstitialcy) for Li atoms were calculated, and we obtained 0.301 eV, 0.297 eV and 1.52 eV, respectively, for the migration energy barrier. The interstitialcy mechanism, where one Li^+ kicks out another Li^+, is deemed to have the closest resemblance

to diffusion mechanisms in amorphous materials, and the energy pathway is plotted as the blue curve in Fig. 4B. For amorphous Li_2O, the effective migration barrier was approximately obtained by the following procedure: first, a super cell with 17 Li atoms and 8 O atoms was taken from the "simulated-annealing" cycles; second, we used this supercell to run *ab inito* MD at 1200 K with a time step of 0.2 fs for more than 10 ps; third, four different local-minimum states were obtained by relaxing MD configurations at 6.6, 6.8, 7.0 and 7.2 ps; Fourth, three CI-NEB calculations, each with eight intermediate steps, were performed among these four continuous local-minimum states, respectively. The resulting pathways are plotted in Fig. 4B in red. From these results, we can roughly identify the effective migration barrier in amorphous Li_2O to be ~0.4 eV.

Further, the displacements of all Li atoms during the MD simulations at 1200 K above were recorded, so the diffusivity of Li^+ at 1200 K was estimated based on the Einstein relation of mean square displacement, $D^{Li} = \lim_{t\to\infty}\{<|\mathbf{r}(t)^{Li} - \mathbf{r}(t=0)^{Li}|^2>/(6t)\}$, as shown in Figure S11. Here all the displacements $\mathbf{r}(t)^{Li}$ were obtained by removing the mass-center displacements of Li atoms. As a result, the diffusivity of Li at 300 K can be obtained based on the migration barrier from NEB calculations and $D^{Li}(T=1200K)$. The results are $D^{Li}(T=1200K) \approx 5.2\times10^{-10}$ m^2/s and $D^{Li}(T=300K) \approx 4.9\times10^{-15}$ m^2/s.

e. Droplet formation along the nanowires

It was frequently observed that ionic liquid based electrolyte (ILE) droplets formed on the nanowires (Fig. 1, S1, S2). Liquid droplets of similar shape on nanowires were already observed in Ref. *S12-S15*, and were postulated to be the aftermath of a Rayleigh like instability (*S15, S16*). These droplets with self-similar shapes (controlled by the competition between the surface energy of the liquid and the liquid-solid interfacial energy) can move and coalesce with each other under the driving force of an electrical field. While this paper may be the first report of the motion of nanoscale liquid droplets observed by in-situ TEM, a detailed discussion of this phenomenon is beyond the scope of this paper. Additional findings regarding nanoscale droplet motion observed by in-situ TEM are planned for a future publication.

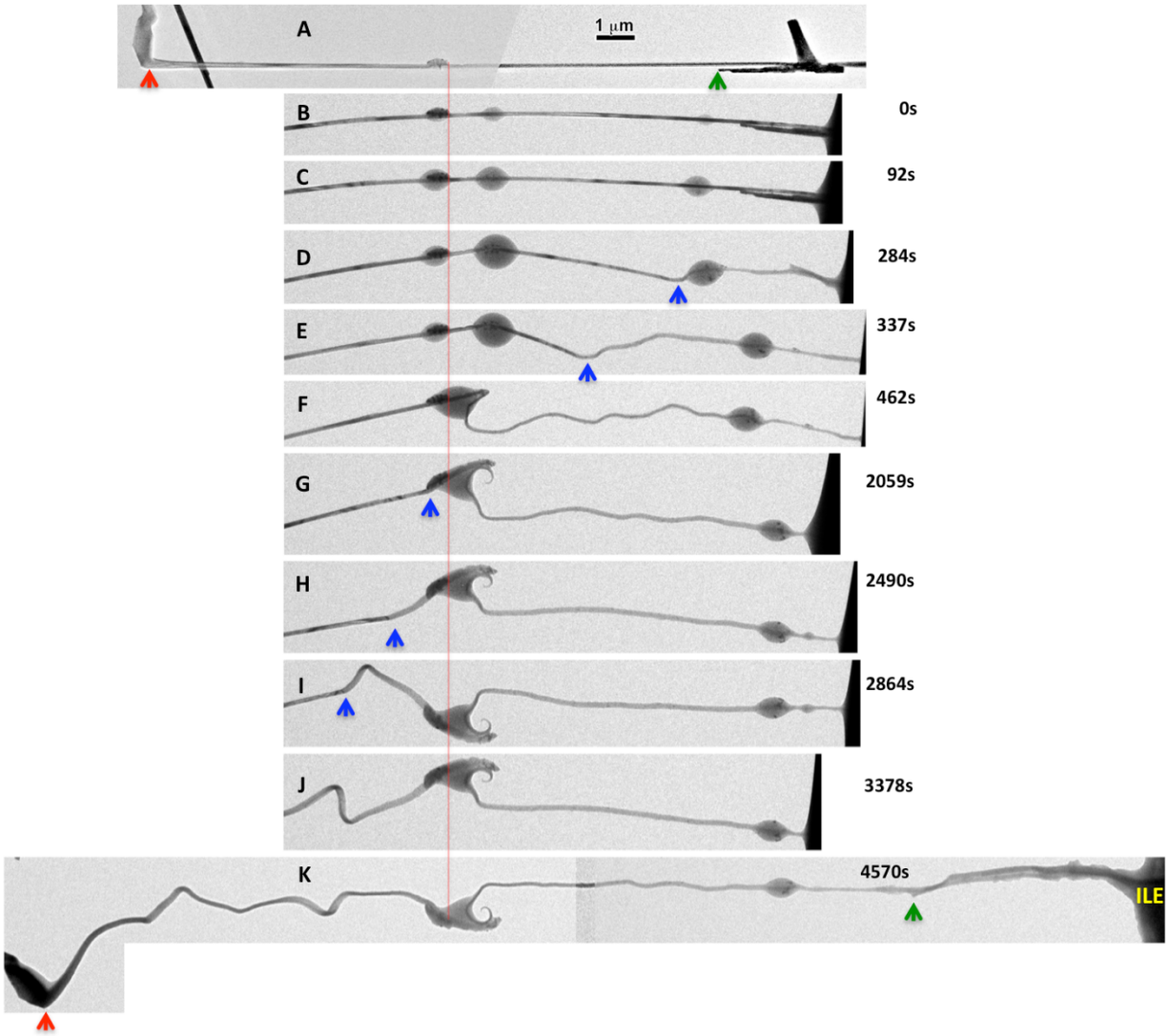

Fig. S1. Time-lapse structural evolution of another SnO_2 nanowire anode during charging at -4 V versus a $LiCoO_2$ cathode. The nanowire was elongated 90% and the diameter increased 35% (volume expansion of 250%) after charging for ~80 minutes (4570s). The initially straight nanowire (**A**) was significantly twisted and bent after charging (**D** to **K**). The reaction front progressed along the nanowire's longitudinal direction, with the front clearly visible as pointed out by arrowheads in (**D** to **I**). The red line in (A) through (K) marks the same feature in the nanowire, which serves as a reference point to track the change of the nanowire length. "ILE" marks ionic liquid-based electrolyte.

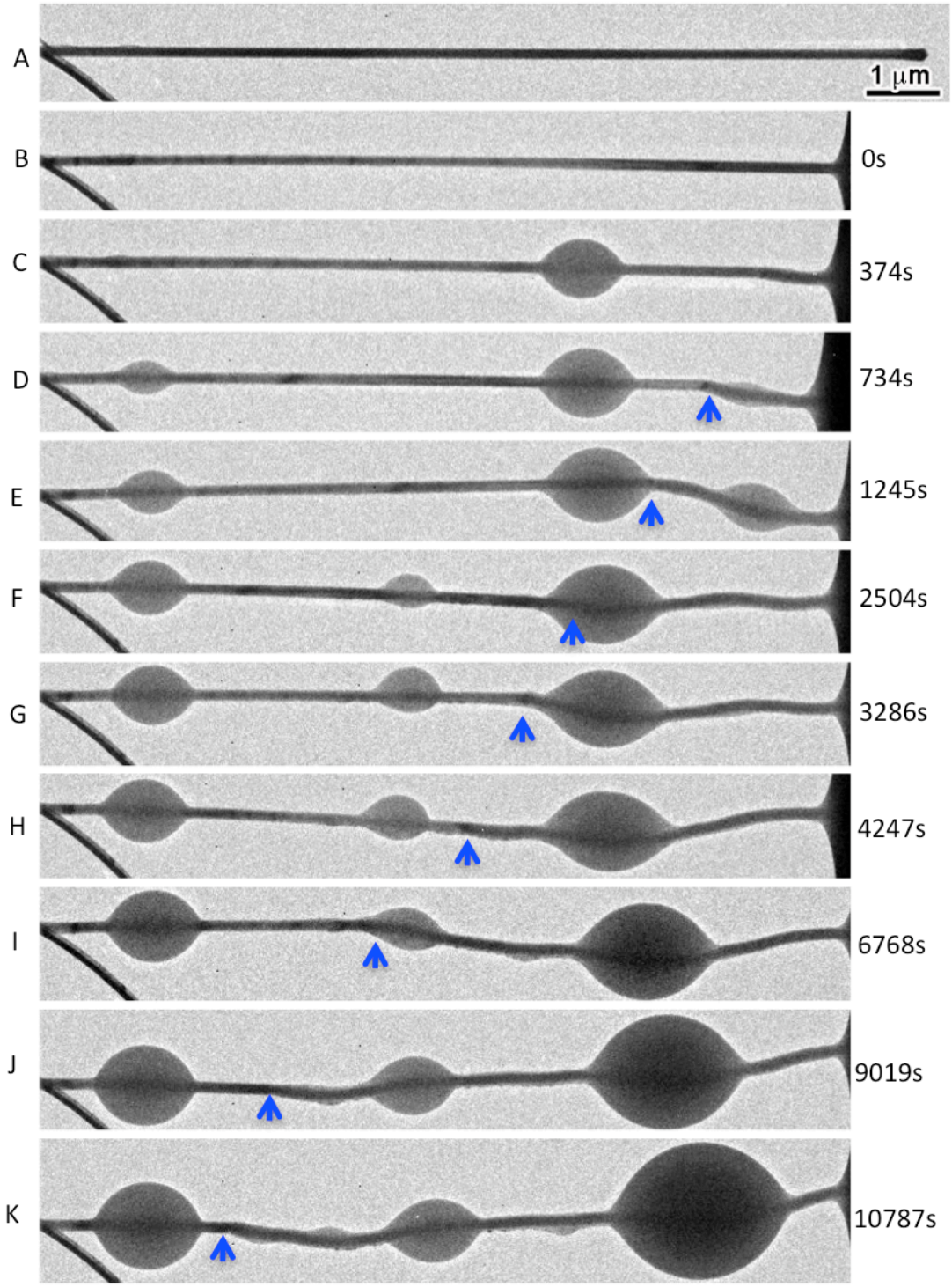

Fig. S2. *In-situ* time-lapsed TEM images of the charging process of a single SnO_2 NW anode. The nanowire was charged at -3 V vs. $LiCoO_2$. (**A**) The initial nanowire. (**B**) The right end of the nanowire was immersed into ILE. (**C** to **K**) The reaction front (marked by arrows) progressed along the longitudinal direction of the nanowire. Multiple beads of ILE were formed on the nanowire.

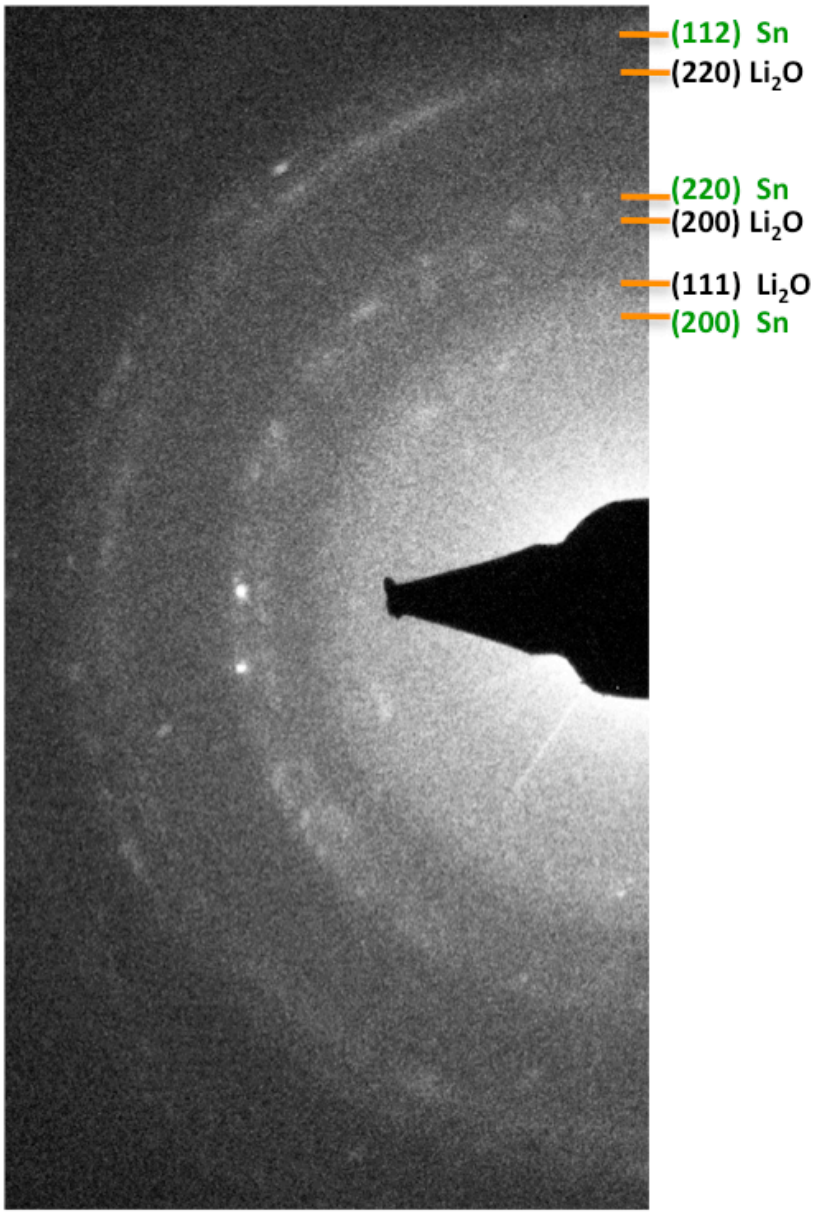

Fig. S3. EDP showing that nanocrystalline Li_2O and nanocrystalline Sn was occasionally observed in the nanowire after the charging reaction.

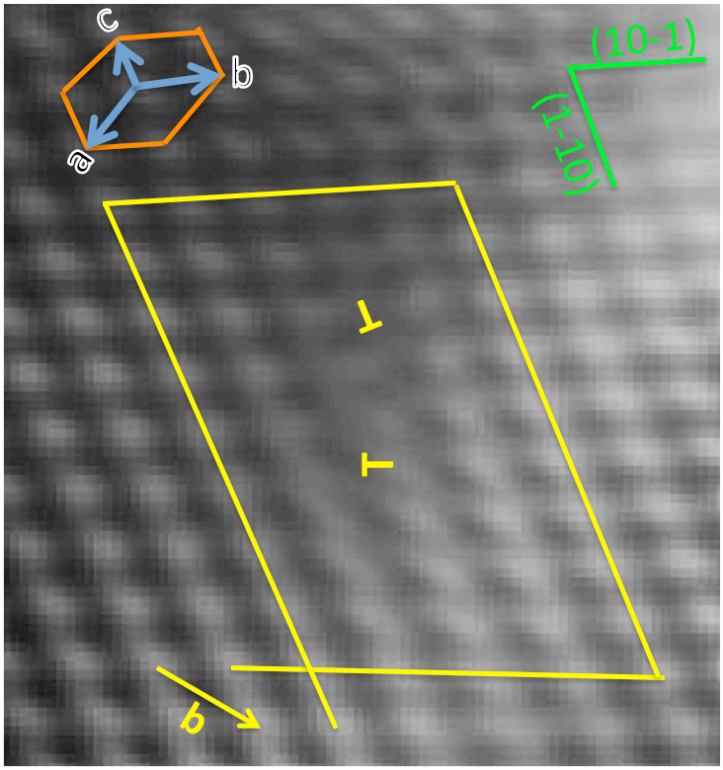

Fig. S4. A HRTEM image showing one type of dislocation generated in the reaction front. The Burgers vector, **b**, of the dislocation was determined to be [01-1], and the slip plane was (100).

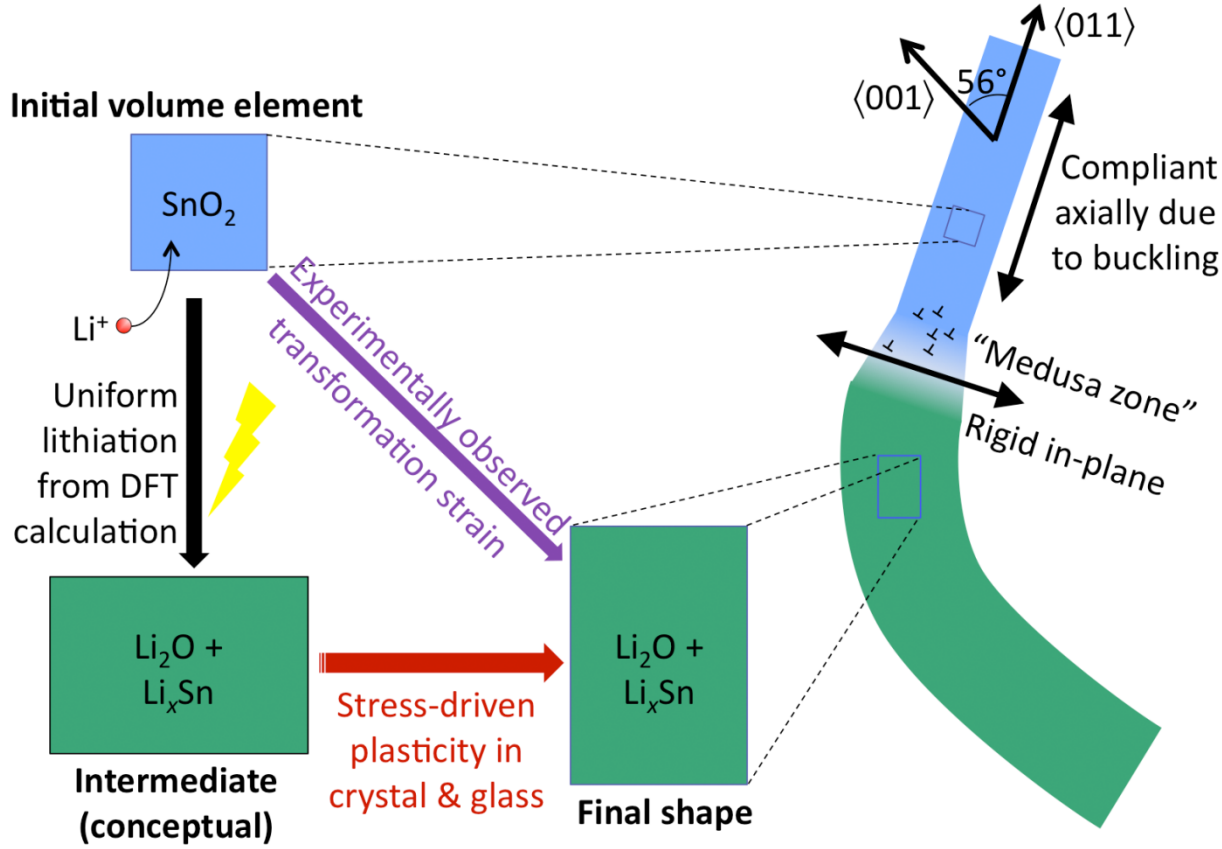

Fig. S5. Nanowire shape change due to coupled electrochemical-mechanical actions. The bold black arrowhead on the left panel indicates shape changes solely due to an electrochemical reaction, which differs from the experimentally-observed shape changes. The experimentally observed shape change is attributed to both the electrochemical reaction and a mechanical plastic deformation, the so-called mechanical and electrochemical coupling effect.

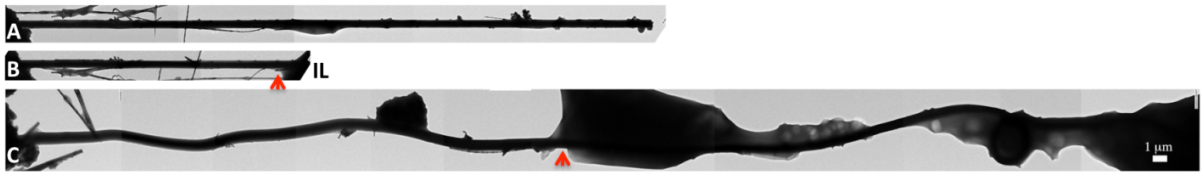

Fig. S6 Morphology changes of a SnO_2 nanowire after charging for 195 minutes at a potential of -3.5 V against a $LiCoO_2$ cathode. Note that the pristine nanowire (A) was partially inserted into the ILE in a "flooded" configuration similar to the scenario in a real battery (B). Arrowheads in (B) and (C) mark the ILE front. Only the segment on the right-hand side of the arrowheads was soaked (flooded) in the ILE. After reaction, the entire nanowire was pulled out of the ILE to inspect the morphology of the flooded segment (C). The elongation, diameter expansion, and total volume expansion of the non-flooded segment were: 100%, 33%, and 254%, respectively, and that of the flooded segment were 96%, 19%, and 178%, respectively. Note that there is significant ILE present on the formerly flooded nanowire surface.

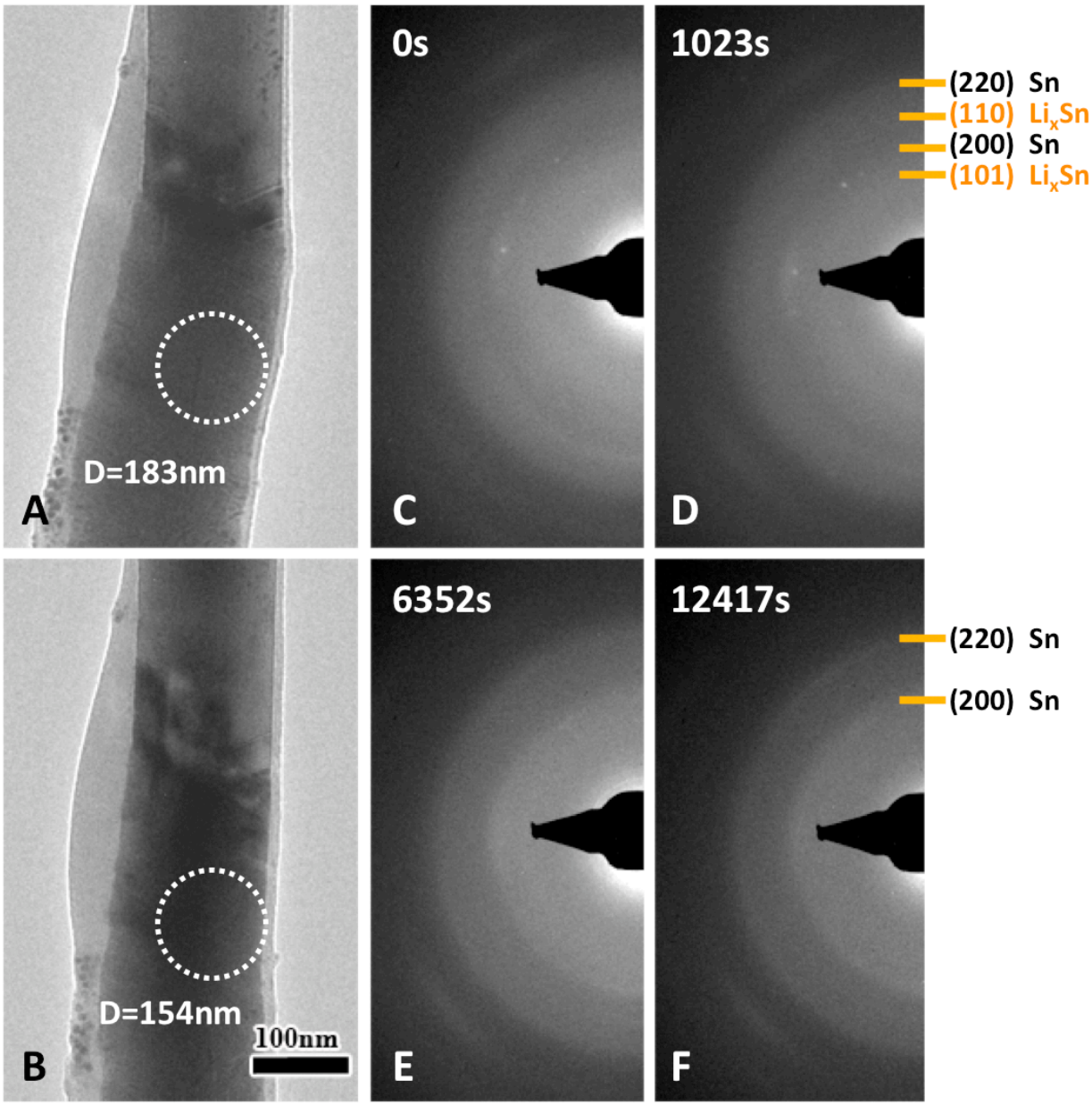

Fig. S7. TEM images of a charged "SnO_2"NW before (**A**) and after (**B**) discharge. The nanowire was biased at -0.05 V versus the $LiCoO_2$ cathode. **(C** to **F)** Time-lapse electron diffraction pattern (EDPs) of the same area as outlined in (A) and (B), showing the structural evolution of the nanowire during discharging. The initial nanowire consisted of Li_xSn, Sn and Li_2O (C and D). After 12417s of discharging, only Sn (diffraction rings in F) and amorphous Li_2O were present (amorphous halo in F). After discharging, the diameter of the nanowire was reduced from 183 nm to 154 nm.

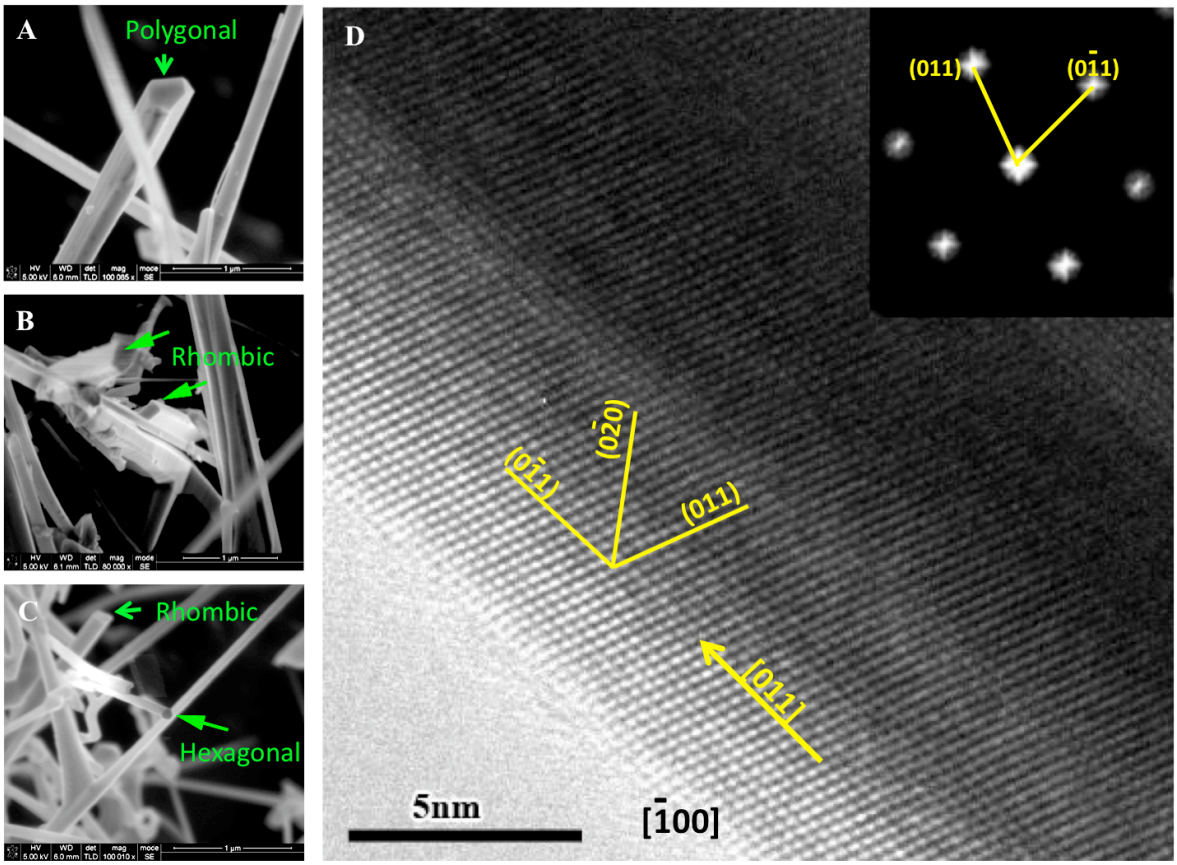

Fig. S8 Cross-section of the nanowire and the growth direction. (A-C) Scanning electron microscopy (SEM) micrographs showing the cross-section of the nanowire is either polygonal (A), or rhombic (B, C), or hexagonal (C). (D) A high resolution transmission electron microscopy (HRTEM) image showing the nanowire growth direction is [011]. Inset is a Fast Fourier Transformation of the HRTEM image.

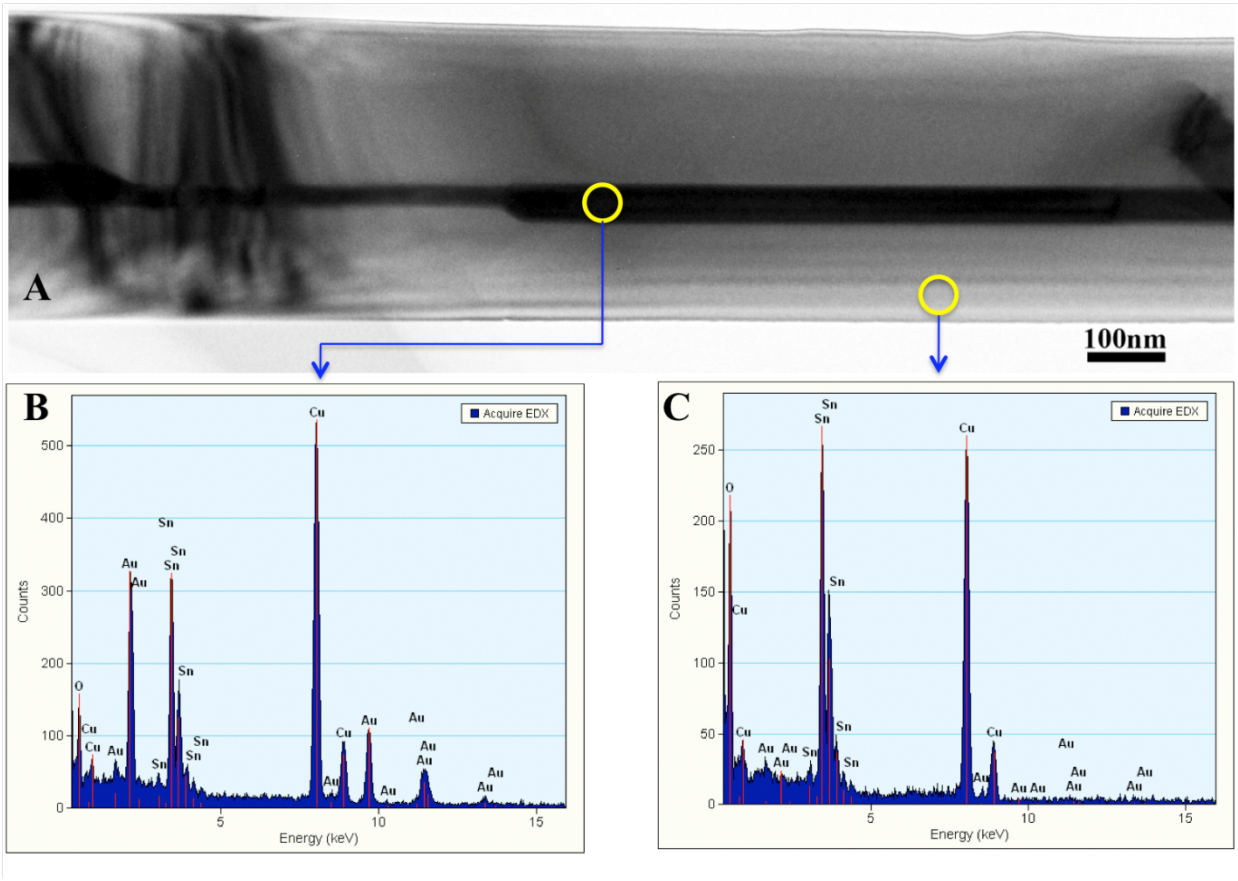

Fig. S9 An as-prepared SnO_2 nanowire with a Au core. (A) A TEM micrograph, (B) Enery-dispersive X-ray spectroscopy (EDX) shows that the core is Au, (C) EDX of the shell is SnO_2.

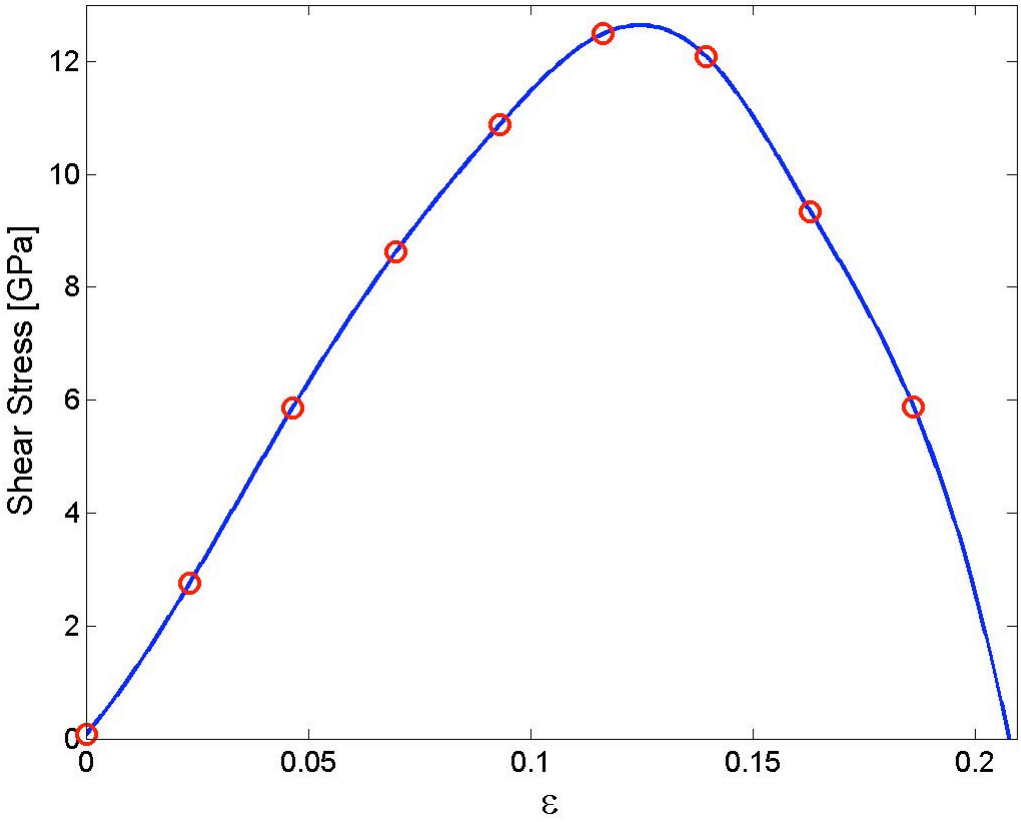

Fig. S10. Relaxed shear stress-strain response of crystalline SnO_2 on the (101) plane along the [-101] shear displacement direction, calculated with DFT.

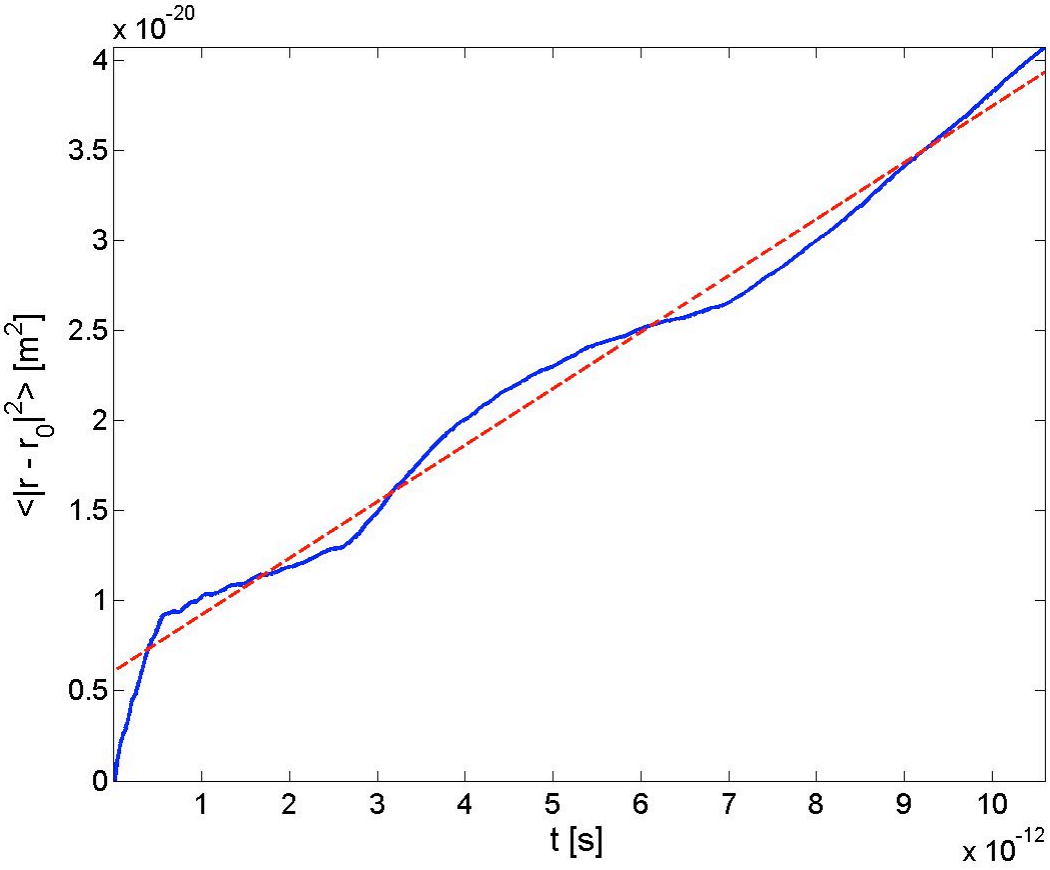

Fig. S11. Mean square displacement of Li atoms in *ab initio* MD simulation of the $Li_{17}O_8$ super cell at 1200 K.

13. **Supporting References**

S1. J. N. Reimers, J. R. Dahn, *Journal of the Electrochemical Society* **139**, 2091 (Aug, 1992).

S2. I. A. Courtney, J. R. Dahn, *J. Electrochem. Soc.* **144**, 2045 (1997).

S3. S. Budak, G. X. Miao, M. Ozdemir, K. B. Chetry, A. Gupta, *Journal of Crystal Growth* **291**, 405 (2006).

S4. J. X. Wang, D. F. Liu, X. Q. Yan, H. J. Yuan, L. J. Ci, Z. P. Zhou, Y. Gao, L. Song, L. F. Liu, W. Y. Zhou, G. Wang, S. S. Xie, *Solid State Communications* **130**, 89 (2004).

S5. G. Kresse, J. Furthmuller, *Physical Review B* **54**, 11169 (1996).

S6. G. Kresse, J. Furthmuller, *Computational Materials Science* **6**, 15 (1996).

S7. P. E. Blochl, *Physical Review B* **50**, 17953 (1994).

S8. J. P. Perdew, K. Burke, M. Ernzerhof, *Physical Review Letters* **77**, 3865 (1996).

S9. H. J. Monkhorst, J.D. Pack, *Physical Review B* **13**, 5188 (1976).

S10. G. Henkelman, H. Jonsson, *Journal of Chemical Physics* **113**, 9978 (2000).

S11. G. Henkelman, B.P. Uberuaga, H. Jonsson, *Journal of Chemical Physics* **113**, 9901 (2000).

S12. W. A. de Heer, P. Poncharal, C. Berger, J. Gezo, Z. M. Song, J. Bettini, D. Ugarte, *Science* **307**, 907 (2005).

S13. H. Kohno, H. Yoshida, J. Kikkawa, K. Tanaka, S. Takeda, *Japanese Journal of Applied Physics Part 1-Regular Papers Brief Communications & Review Papers* **44**, 6862 (2005).

S14. L. Song, A. W. Holleitner, H.H . Qian, A, Hartschuh, M. Dolinger, E. M. Weig, J. P. Kotthaus, *Journal of Physical Chemistry C* **112**, 9644 (2008).

S15. S. Dawar, G. G. Chase, *Separation and Purification Technology* **60**, 6 (2008).

S16. A. G. Gonzalez, J. A. Diez, R. Gratton, D. M. Campana, F. A. Saita, *Journal of Fluid Mechanics* **651**, 117 (2010).

MATERIALS SCIENCE

Building a Better Battery

Controlling the charge-induced morphological changes of electrode materials may provide a route to improved battery performance.

Yet-Ming Chiang

Innovations in the battery field are infrequent and hard-won. New electrochemical systems (a new positive or negative electrode, electrolyte, or combination thereof) reach the marketplace only once every few years, and the energy density of lithium-ion batteries as a class has increased on average by only 8 to 9% per year since the early 1990s. Thus, in the burgeoning field of nanoscale electrode materials, skepticism regarding new claims is perhaps not surprising because of the many requirements that any battery electrode must simultaneously meet to be commercialized. One route by which battery performance can be compromised is by mechanical failure due to the large volume changes associated with the charge-discharge cycle. On page 1515 of this issue, Huang *et al*. (*1*) report an ingenious in situ transmission electron microscope (TEM) experiment that uses a low–vapor pressure ionic liquid electrolyte to allow imaging of a SnO_2 nanowire electrode in an "open" electrochemical cell. They observe a reaction mechanism in the SnO_2 nanowires that progresses sequentially along the nanowire from end to end, allowing them to accommodate a ~250% volume change without fracturing and at practical charging rates. These intriguing results raise the question of whether such one-dimensional phase transformations can be induced in other materials.

Nanomaterials offer the promise of high storage capacity at useful current rates, along with reversible cycling over hundreds to thousands of cycles and over a wide temperature range. However, there are practical concerns specific to nanomaterials: Nanoparticle electrodes may have low packing density that makes high bulk energy density difficult to realize; synthesis methods may not be scalable and/or economical in a field where cost is a most important metric (e.g., electric vehicle and grid storage batteries); and nanoscale forms of inherently reactive compounds raise questions of safety and stability. There are also fundamental scientific questions centered on the mechanisms of electrochemical storage because of departures from known scaling laws as the size scale decreases. All of these issues need to be convincingly and simultaneously addressed if laboratory-based results are to be successfully translated into substantial progress in battery performance.

SnO_2 is a model for a class of metal oxides and fluorides (*2*–*4*) in which reversible storage capacities exceeding those possible with intercalation reactions are realized with displacement or "conversion" reactions that produce one or more new phases. Electrochemical reduction of the starting oxide by lithium produces Li_2O [LiF in the case of the fluorides (*4*)] and the parent metal, but unlike primary battery systems such as Li/MnO_2 that undergo the same reaction but are poorly reversible, reversible storage has been obtained when the product phases are nanoscale and reactive. In the case of SnO_2, the Li_2O reaction product does not participate in reversible storage; subsequent cycling stores lithium through an alloying reaction with the nanoscale particles of metallic Sn. This was first established in SnO_2-bearing glasses (*5*) and is also the case for Huang *et al*.'s nanowires. Thus, this reaction mechanism has the drawback of a large and irreversible loss of working lithium in the first cycle, whereas in other systems the conversion reaction produces nanoscale Li_2O or LiF that does react reversibly with the metal electrode and is the main contributor to reversible capacity (*2*, *4*). However, the large strain accommodation capability shown by the SnO_2 nanowires would be valuable if achievable in other high-capacity, high-strain electrodes such as silicon. Alloying with Li to the limiting composition $Li_{4.4}Si$ yields theoretically an enormous capacity of 4200 milliampere hours per gram (mAh/g), versus 150 mAh/g for $LiCoO_2$ cathodes and 350 mAh/g for graphite anodes used in conventional lithium-ion batteries, but also produces a molar volume change of 311%. Silicon undergoes solid-state amorphization during lithiation (*6*), and one strategy for strain accommodation is to limit the extent of lithiation (which sacrifices charge storage capacity) to maintain an amorphous phase (*7*). Silicon nanowires, on the other hand, have exhibited reversible capacities exceeding 3000 mAh/g (*8*).

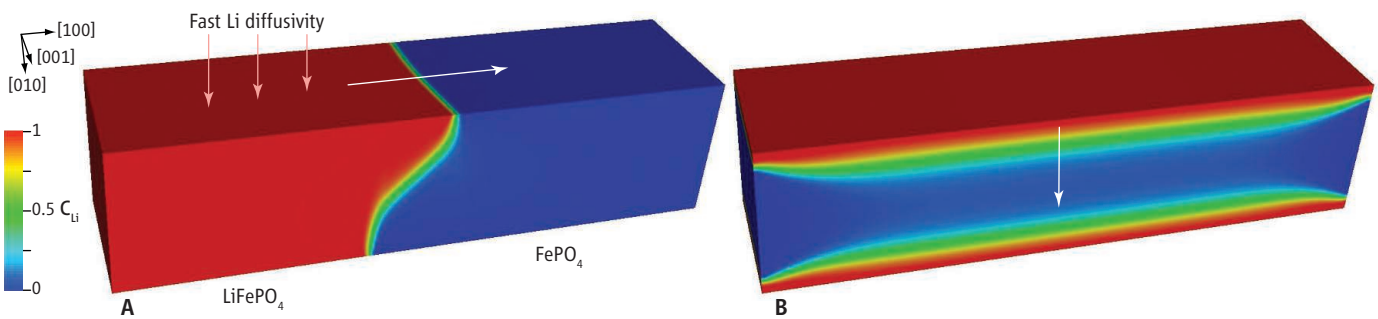

Coping with strain. (**A**) Phase field modeling reveals that under a moderate overpotential of 25 mV, misfit stress causes $FePO_4$ to grow along the [100] longitudinal direction, normal to the fast-diffusion direction. (**B**) Increasing the overpotential to 100 mV allows Li diffusion anisotropy to dominate the transformation morphology; diffuse phase boundaries migrate inward along the [010] direction. C_{Li}, lithium concentration

In considering how one-dimensional transformation morphologies might be induced, an example from the first successfully commercialized nanoscale cathodes, the phospho-olivines, may be instructive. Strain accommodation (*9*, *10*) and related phase transformation kinetics (*11*) are tunable features of nanoscale olivines and have been implicated as design criteria for high-power and long cycle life. The figure shows results using a phase-field model (*12*) to simulate possible transformation morphol-

Department of Materials Science and Engineering, Massachusetts Institute of Technology, Cambridge, MA 02139, USA. E-mail: ychiang@mit.edu

Published by AAAS

ogies in a $LiFePO_4$ nanorod during the first-order phase transition to $FePO_4$. The anisotropy of Li diffusion and the magnitude of misfit strain (~7% volume strain) have been explicitly included, and the driving force for the transformation is varied via the electrical overpotential (*13*). At a moderate overpotential of 25 mV (see the figure, panel A), stress relaxation causes $FePO_4$ to grow along the [100] longitudinal direction, analogous to that of Huang *et al*., even though Li diffusion is fastest normal to this direction. However, at a higher overpotential of 100 mV, the influence of strain energy is overcome and lateral Li diffusion dominates the transformation morphology (see the figure, panel B).

Thus, interactions among stress, transport anisotropy, and the magnitude of the driving force (among other variables) may influence phase transformation morphology in nanowire electrodes. Other unanswered questions include the effect of electrolyte distribution: Is the one-dimensional transformation in SnO_2 facilitated by having a thin wetted layer of electrolyte, and would results differ for a "flooded" electrolyte battery? And could a competing radial reaction morphology also preserve the nanowire morphology? Regardless, the results presented by Huang *et al*. are testimony to the power of direct observation in electrochemical materials science, and they illustrate a previously unrecognized mode of reaction in battery electrodes. The results should stimulate others to consider analogous experiments and mechanisms in other storage materials, and should contribute to the design of nanoscale electrodes that fully exploit the potential of ultrahigh-capacity storage materials.

References

1. J. Y. Huang *et al*., *Science* **330**, 1515 (2010).
2. P. Poizot, S. Laruelle, S. Grugeon, L. Dupont, J.-M. Tarascon, *Nature* **407**, 496 (2000).
3. H. Li, P. Balaya, J. Maier, *J. Electrochem. Soc.* **151**, A1878 (2004).
4. G. G. Amatucci, N. Pereira, *J. Fluor. Chem.* **128**, 243 (2007).
5. Y. Idota, T. Kubota, A. Matsufuji, Y. Maekawa, T. Miyasaka, *Science* **276**, 1395 (1997).
6. P. Limthongkul, Y.-I. Jang, N. J. Dudney, Y.-M. Chiang, *Acta Mater.* **51**, 1103 (2003).
7. M. N. Obrovac, L. J. Krause, *J. Electrochem. Soc.* **154**, A103 (2007).
8. C. K. Chan *et al*., *Nat. Nanotechnol.* **3**, 31 (2008).
9. G. Chen, X. Song, T. Richardson, *Electrochem. Solid-State Lett.* **9**, A295 (2006).
10. N. Meethong, H.-Y. S. Huang, S. A. Speakman, W. C. Carter, Y.-M. Chiang, *Adv. Funct. Mater.* **17**, 1115 (2007).
11. N. Meethong, Y.-H. Kao, W. C. Carter, Y.-M. Chiang, *Chem. Mater.* **22**, 1088 (2010).
12. M. Tang, W. C. Carter, Y.-M. Chiang, *Annu. Rev. Mater. Res.* **40**, 501 (2010).
13. Y.-H. Kao *et al*., *Chem. Mater.* **22**, 5845 (2010).

10.1126/science.1198591

PLANT SCIENCE

Genome Evolution in Plant Pathogens

Pathogen genes that shut down specific host plant immune responses are highly divergent and have evolved rapidly to accommodate adaptation.

Peter N. Dodds

Food security is of global importance and crop diseases caused by plant pathogens are a major constraint to agriculture worldwide. Many of these pathogens have a similar biotrophic life stage during which they contact host cells and secrete effector proteins that alter plant responses to infection (*1*). In this issue, comparative genomics studies of closely related pathogen species by Raffaele *et al*. on page 1540 (*2*), Baxter *et al*. on page 1549 (*3*), Spanu *et al*. on page 1543 (*4*), and Schirawski *et al*. on page 1546 (*5*) reveal that such effector proteins evolve rapidly and that their diversity contributes to host range and parasite speciation.

Biotrophic infection strategies have evolved independently in diverse lineages of plant pathogens. These include fungus-like parasites (oomycetes) from the kingdom Stramenopila, such as the destructive potato blight pathogen *Phytophthora infestans* (agent of the Irish potato famine), fungi such as powdery mildews (ascomycetes), and rust and smut fungi (basidiomycetes). These pathogens form specialized hyphae (called haustoria) that penetrate the plant cell wall and allow nutrient uptake from host tissue (*6*). These structures also secrete large repertoires of effector proteins that enter host cells and manipulate defense responses and cellular metabolism. Many oomycete effectors require the short amino acid motif RxLR (Arg, any amino acid, Leu, Arg) for entry into plant cells (*7*), independently of other pathogen machinery (*8*, *9*). Some fungal effectors also enter host plant cells (*10*, *11*), although they lack clearly conserved peptide motifs.

Agricultural threats. Many pathogens, such as *Phytophthora infestans*, target major food crops, such as potato (shown). The genes involved in host-pathogen interactions are highly diversified among related *Phytophthora* species that attack different plants.

Raffaele *et al*. compared the genomes of four very closely related *Phytophthora* species that infect quite different host plant species (see the figure). The evolution of these pathogens therefore involved relatively recent shifts in host range, followed by specialization to the new hosts. They found most pathogen genes and genome regions to be highly conserved, but genes involved in host-pathogen interaction appear highly diversified, especially the predicted RxLR-containing effectors. Most of these genes are located in gene-sparse, transposon-rich genome regions, suggesting that these features allow rapid evolution of effector loci after host changes. Genes involved in chromatin modification are also located in these regions and show extensive variation, suggesting that epigenetic regulation of gene expression also contributes to adaptation following host shifts.

Despite having a biotrophic life stage, *Phytophthora* species subsequently kill the infected parts of the plant but continue to feed on the dead plant tissue (and can be cultured on simple medium). By contrast, the related oomycete *Hyaloperonospora arabidopsidis*, which is a pathogen of the model plant *Arabidopsis thaliana*, is exclusively biotrophic and cannot be grown in culture. This pathogen is believed to have evolved from a *Phytophthora*-like hemibiotrophic ancestor. Baxter *et al*. found that its genome contains a unique set of diversified RxLR-containing effectors but has lost many of the hydrolytic

Division of Plant Industry, Commonwealth Scientific and Industrial Research Organisation, Canberra, ACT 2614, Australia. E-mail: peter.dodds@csiro.au